Process optimization for zero-liquid discharge desalination of shale gas flowback water under uncertainty

Viviani C. Onishi [a,] *, Rubén Ruiz-Femenia [a], Raquel Salcedo-Díaz [a], Alba Carrero-Parreño [a], Juan A. Reyes-Labarta [a], Eric S. Fraga [b], José A. Caballero [a]

[a] *Institute of Chemical Process Engineering, University of Alicante, Ap. Correos 99, Alicante 03080, Spain*

[b] *Centre for Process Systems Engineering, Department of Chemical Engineering, University College London, London WC1E 7JE, UK*

***** Corresponding author at**. *Institute of Chemical Process Engineering, University of Alicante, Ap. Correos 99, Alicante 03080, Spain. Phone: +34 965903400. E-mail addresses: viviani.onishi@ua.es / viviani.onishi@pq.cnpq.br (Viviani C. Onishi).*

ABSTRACT

Sustainable and efficient desalination is required to treat the large amounts of high-salinity flowback water from shale gas extraction. Nevertheless, uncertainty associated with well data (including water flowrates and salinities) strongly hampers the process design task. In this work, we introduce a new optimization model for the synthesis of zero-liquid discharge (ZLD) desalination systems under uncertainty. The desalination system is based on multiple-effect evaporation with mechanical vapor recompression (MEE-MVR). Our main objective is energy efficiency intensification through brine discharge reduction, while accounting for distinct water feeding scenarios. For this purpose, we consider the outflow brine salinity near to salt saturation condition as a design constraint to achieve ZLD operation. In this innovative approach, uncertain parameters are mathematically modelled as a set of correlated scenarios with known probability of occurrence. The scenarios set is described by a multivariate normal distribution generated via a sampling technique with symmetric correlation matrix. The stochastic multiscenario non-linear programming (NLP) model is implemented in GAMS, and optimized by the minimization of the expected total annualized cost. An illustrative case study is carried out to evaluate the capabilities of the proposed new approach. Cumulative probability curves are constructed to assess the financial risk related to uncertain space for different standard deviations of expected mean values. Sensitivity analysis is performed to appraise optimal system performance for distinct brine salinity conditions. This methodology represents a useful tool to support decision-makers towards the selection of more robust and reliable ZLD desalination systems for the treatment of shale gas flowback water.

Keywords: Shale gas flowback water; Multiple-effect evaporation with mechanical vapor recompression (MEE-MVR); Zero-liquid discharge (ZLD); Uncertainty; Risk management; Robust design.

1. Introduction

Shale gas production is a promising energy source to address the increasing global demand. Advances in horizontal drilling and hydraulic fracturing ("*fracking*") technologies allied to economic factors that include supply reliability, have driven growth in unconventional natural gas production from shale reserves (Cooper et al., 2016; Xiong et al., 2016). In the United States (U.S.), recent projections of the Energy Information Administration indicate that shale gas can reach 30% of all natural gas produced in the world by 2040 (EIA, 2016a, 2016b). Notwithstanding, one of the biggest challenges for promoting further development and cleaner production of shale gas relies on optimal management of flowback water (Vidic et al., 2013). This is mainly due to the large amounts of high-salinity wastewater generated during shale gas extraction (Huang et al., 2016).

Drilling and fracking of horizontal wells requires elevated quantities of water-based fracturing fluid to create a fractures network, and release gas trapped into tight shale formations (Chen and Carter, 2016). Depending on the shale rocks characteristics, gas exploration of one single well demands between 10 500–21 500 m^3 (~3–6 million gallons) of water (Ghanbari and Dehghanpour, 2016; Jacquet, 2014). However, other authors suggest this amount can be even higher, reaching 30 000 m^3 (~8 million gallons) per well completion (Hammond and O'Grady, 2017). The injection fluid is predominantly constituted by proppant (sand and water mixture, ~98%) and chemical enhancers (corrosion inhibitors, friction reducers, surfactants, flow improvers, *etc.*) (Stephenson et al., 2011). Several reports indicate a range of 10–80% of the total amount of fracking fluid that returns to ground as flowback water, during the first two weeks from well operations start (Hammond and O'Grady, 2017; Slutz et al., 2012). **Table 1** presents shale gas flowback water information and average water amounts needed for horizontal drilling and hydraulic fracturing processes in prominent U.S. shale plays.

For lessening environmental damage, shale gas flowback water should be reclaimed to be recycled or reused as injection fluid for new wells exploitation. In any case, shale gas wastewater demands specific pre-treatment—that comprises filtration, physical and chemical precipitation, flotation and sedimentation—and effective desalination to allow its reuse or safe disposal (Carrero-Parreño et al., 2017). In addition to chemical additives and other pollutants (*e.g.*, organic matter, particulates, greases, and radioactive elements, to name a few) (Vengosh et al., 2013), hypersaline concentrations in shale gas flowback water can be hazardous to human health and the environment (Vengosh et al., 2014). Desalination technologies should play a key role in hydrological planning schemes for optimal water resources management in shale gas production.

Due to aforementioned reasons, advanced and more efficient technologies for flowback water desalination should be developed for enhancing general sustainability and efficiency in shale gas industry (Onishi et al., 2017a; 2017b). Nevertheless, great uncertainty associated with well data (including flowback water flowrates and salinities) strongly hampers the optimal process design. Generally, a deterministic approach (*i.e.*, system design and optimization considering a single set of process inlet conditions) cannot provide all required system flexibility under process parameters variability. This methodology could lead to weak system performance represented by sub-optimal solutions, when considering different feeding scenarios. In addition, this approach does not provide any information to the decision maker on the impact of uncertain parameters on the design chosen.

Design and optimization under uncertainty have received increased interest by the literature in last years (see Sahinidis (2004) for general information about the subject).

Some authors have directed their efforts to optimize water management in shale gas process under uncertainty. For instance, Yang et al. (2014) have presented an stochastic model for optimizing shale gas fracturing schedule, in accordance to water transportation, and wastewater treatment and reuse, by considering uncertain water availability. In Zhang et al. (2016), a mathematical model has been proposed to determine the optimal flowback water treatment and disposal options for water management during shale gas operations. In their work, the data uncertainty is modelled via a hybrid fuzzy-stochastic approach. Additional notable contributions are addressed by Gao and You (2015) and Lira-Barragán et al. (2016). In spite of these attempts to optimize water management, research about shale gas flowback water desalination under uncertainty is still in its first steps.

Different desalination processes can be applied for desalination of high-salinity wastewater, which encompasses membrane and thermal-based technologies. The first group includes reverse osmosis (RO) and multistage membrane distillation (MD), while the second one comprises multistage flash distillation (MSF) and single/multiple-effect evaporation systems with/without mechanical or thermal vapor recompression (SEE/MEE-MVR/TVR). In a recent study, Boo et al. (2016) have experimentally evaluated the performance of direct contact MD for the shale gas wastewater desalination, by using a modified omniphobic membrane. Also, Jang et al. (2017) have evaluated the suitability of three different desalination techniques for salt removal from shale gas wastewater: MD, RO and evaporative crystallization (EC). Their results show relatively higher efficiencies for MD and EC in comparison with the RO process. According to Shaffer et al. (2013), multiple-effect evaporation with mechanical vapor recompression (MEE-MVR) processes are frequently more advantageous than membrane-based processes for shale gas wastewater applications. As a consequence of lower susceptibility to fouling and rusting problems, MEE-MVR systems often require less intensive pre-treatment processes.

Michel et al. (2016) have performed an experimental study on pre-treatment and desalination of shale gas flowback water. The authors have considered a two-stage treatment process composed by pre-treatment technologies (filtration, pH adjustment, oxidation and sedimentation) and posterior nanofiltration/RO desalination. Results obtained in their work emphasize the need for very effective pre-treatment before membrane desalination becomes possible. Cho et al. (2016) have studied the application of anti-scalants to diminish scale formation in MD desalination of flowback water from shale gas fracking. Note that other benefits of MEE desalination systems are related to facility of scaling and dealing with non-condensable gases (Shen et al., 2015), in addition to a lower operation temperature that reduces equipment sizing and insulation (El-Dessouky and Ettouney, 1999). Although previous studies represent important improvements for shale gas wastewater treatment, none of them has contemplated zero-liquid discharge (ZLD) operation.

A ZLD process has been investigated by Thu et al. (2015), through multiple-effect adsorption applied to seawater desalination. Tong and Elimelech (2016) have critically reviewed the driving forces, technologies and environmental impacts of ZLD as an prominent strategy for wastewater management. In their work, the authors have examined the advantages and limitations of both membrane and thermal-based ZLD technologies. Chung et al. (2016) have proposed multistage vacuum membrane distillation for ZLD desalination of high-salinity water. The latter authors have used a finite differences-based method for the numerical simulation of the process, by allowing salt concentration in brine discharges near to saturation condition. On the other hand, Han et al. (2017) have developed mathematical models for SEE and MEE-MVR processes simulations of ZLD seawater desalination. Through energy and exergy analyses, the authors have concluded that MEE are often more attractive than single-effect systems, due to lower compressor power consumption. However, their study lacks a comprehensive cost analysis.

For addressing the application of ZLD to shale gas flowback water desalination, Onishi et al. (2017b) have developed a mathematical model for optimal design of SEE/MEE systems with single or multistage MVR and heat integration. The non-linear programming (NLP) model has been based on a general superstructure, including feed pre-heating, multiple evaporation effects with flash separation and multistage intercooling compression. Still, the authors have performed a thorough comparison between the optimal SEE/MEE (with/without multistage compression) systems configurations obtained, in terms of their capability to produce freshwater and achieve ZLD conditions under different wastewater inlet salinities. Energy and economic analyses indicate the MEE process with single-stage compression as the most cost-effective process for desalting shale gas flowback water. With this important result in mind, Onishi et al. (2017a) have proposed a new rigorous optimization approach by the consideration of a more accurate calculation of heat transfer coefficients. Moreover, the authors have included the modelling of major equipment features, which allows the estimation of the optimal number and length of tubes, and the shell diameter of the evaporator. Then, uncertainty related to data from shale gas can be considered during the design task of the above-mentioned processes for improving system flexibility and robustness.

Into this framework, we introduce a new mathematical model for optimal design of ZLD evaporation systems under correlated data uncertainty. The multistage superstructure is defined by multiple-effect evaporation process with heat integration and mechanical vapor recompression (MEE-MVR). The MEE-MVR process is based on our previous study (Onishi et al., 2017b), in which the system is composed of several evaporation effects with horizontal falling film tubes coupled to flashing tanks and an electric-driven compressor. Our main goal is energy efficiency intensification of shale gas flowback water desalination through lessening brine discharges, while accounting for distinct water feeding scenarios. For this purpose, ZLD process is ensured by a design constraint that defines the outflow brine salinity near to the salt saturation condition—note that, under the latter restriction, the proposed MEE-MVR system will technically achieve brine discharges close to ZLD conditions. Brine crystallizer or evaporation ponds are still required to remove remaining water amounts from the brine to reach the real ZLD condition—. To the best of our knowledge, this is the first study assessing the impacts of data uncertainty on the optimal design of ZLD evaporation systems, specially developed for shale gas flowback water desalination. Furthermore, we emphasize that important improvements on the process are implemented, including the use of an external energy source to avoid oversized equipment.

In this new approach, feed water salinity and flowrate are both considered as uncertain design parameters. These uncertain parameters are mathematically modelled as a set of correlated scenarios with given probability of occurrence. Scenarios generated by MATLAB are described by multivariate normal distribution, via sampling technique based on symmetric correlation matrix. The stochastic multiscenario NLP-based model is optimized in GAMS, through the minimization of the expected total annualized cost. An illustrative case study is performed to evaluate the capabilities of the proposed new modelling stochastic methodology. Cumulative probability curves are constructed for the assessment of financial risk associated with the uncertain parameters space for different standard deviations of mean values. Additionally, sensitivity analysis is carried out to appraise optimal system performance for distinct brine salinity conditions.

This paper is organized as follows: In **Section 2**, we properly define the problem of interest. **Section 3** presents the detailed description of the MEE-MVR superstructure proposed for the desalination of shale gas flowback water. The stochastic multiscenario NLP model is developed in **Section 4**, while the scenario generation is explained in **Section 5**. The impact of uncertainty on MEE-MVR system design is assessed in **Section 6**, using a shale gas case study based on uncertain real data. Finally, we summarize the main conclusions in the **last section**.

2. Problem statement

The problem of interest is formally stated as follows. Given is a stream of high-salinity shale gas flowback water, which requires effective desalination treatment. The shale gas flowback water stream has known inlet conditions (defined by its temperature, pressure and uncertain salinity and flowrate) and a target state described by the ZLD brine discharge specification (*i.e.*, 300 g kg^{-1}). In addition, a MEE-MVR desalination system (composed by multiple-effect evaporator, flashing tanks, preheater, mechanical compressor, mixers and pumps) and energy services (electricity and steam) are also provided with their corresponding costs. The main objective is to achieve energy efficiency intensification of flowback water desalination process by lessening brine releases, while accounting for distinct water feeding scenarios. Furthermore, we consider that both salinity and flowrate of shale gas flowback water are uncertain design parameters that can be expressed through different correlated scenarios (each one presenting different water feeding conditions). Note that the data uncertainty is associated with the great variability presented in data of salt concentrations and flowrates of wastewater from shale plays. The general superstructure proposed for the optimization of MEE-MVR desalination process is displayed in **Fig. 1**.

Shale gas flowback water desalination can be performed after specific pre-treatment to remove suspended solids, oils, greases and chemical additives. Further information about efficient pre-treatment processes applied to shale gas flowback water is presented in Carrero-Parreño et al. (2017). In this case, we assume that shale gas flowback water remains with elevated concentration of salts after its pre-treatment. Thus, the optimal MEE-MVR system design should correspond to the most cost-effective desalination process, exhibiting reduced brine releases and high freshwater production in all scenarios. We highlight that energy intensification allied to ZLD operation allows the reduction of environmental impacts related to energy consumption and wastewater disposal. For achieving the goals of ZLD process and high freshwater production, we intend to optimize the MEE-MVR system performance under uncertainty, through the minimization of the expected total annualized cost. The objective function accounts for the contributions related to capital investment in equipment (scenario independent variable), and operational expenses regarding electricity and vapor consumption (scenario-dependent variables). Moreover, the optimal ZLD operation in the uncertain search space is ensured by including a design constraint that defines brine discharge salinity near to salt saturation conditions in each scenario.

The MEE-MVR system optimization for ZLD desalination of shale gas wastewater under uncertainty is a very difficult task, aimed at obtaining the optimal system configuration and operational conditions for distinct feeding scenarios. Hence, the optimal MEE-MVR system should have lower equipment size (represented by heat transfer areas and compressor capacity) and minimum thermal services (electric power and steam) consumption. Nonetheless, at the same time, the MEE-MVR system should be able to efficiently operate in a large range of correlated scenarios. For this purpose, the decision variables are divided into two sets: the scenario independent and scenario-dependent variables. The first set is not influenced by uncertain parameters, while the second one is sensitive to the uncertainty in the search space. Sahinidis (2004) have pointed out scenario-dependent variables as a recourse against any infeasibility that would arise from a particular materialization of the uncertainty. Typically, equipment sizes are scenario independent optimization variables. On the other hand, all streams properties and operating conditions—which include specific enthalpy, specific heat, temperature, pressure, salinity and flowrate—are unknown scenario-dependent variables requiring optimization. **Fig. 2** displays the main decision variables for the optimization of: (*a*) single-stage compressor; and, (*b*) effect *i* of the evaporator coupled to flashing tank *i* in the MEE-MVR system.

The MEE-MVR system should be operated at low pressures and temperatures to avoid instability and prevent fouling and rusting problems. For this reason, upper and lower bounds on temperature and pressures for all feeding scenarios are essential to solve the problem. Besides the increased number of optimization variables and constraints to guarantee proper system functioning, the high non-convexity and nonlinearity of some modelling equations and cost correlations add further complexity to the model. It should be observed that physical properties, as well as boiling point elevation (BPE), are functions of streams temperature and salinity that should also be estimated in all scenarios as shown in **Appendix A**.

3. Superstructure and process description

The MEE-MVR superstructure proposed for the shale gas flowback water desalination is essentially composed of the following equipment:

(i) Horizontal falling film evaporator with multiple effects.

(ii) Flashing tank separators.

(iii) Single-stage mechanical vapor compressor.

(iv) Shell-and-tube heat exchanger.

(v) Mixers and pumps.

As illustrated in **Fig. 1**, the MEE-MVR desalination system presents several evaporation effects coupled to a mechanical vapor compressor and intermediate flashing tank separators. It is worth to mention that each evaporation effect is composed of a tube-bundle containing numerous horizontal falling film tubes, demister for droplets separation and spray nozzles. These equipment pieces are housed inside the shell that should also have space for saturated vapor and brine concentrate pool. The vapor condensation occurs inside the horizontal-tubes, while feeding is sprayed onto the tube-bundle to produce a thin film for water evaporation. Thus, the vapor condensation starts by absorbing latent heat from the falling film outside tubes. In an opposite way, vaporization occurs due to the latent heat transferred from condensed vapor in the tube-side. In the first evaporation effect, the condensate temperature is changed by transferring its sensible heat. As a result, this variable is decreased from its inlet superheated condition to the outlet temperature corresponding to vapor saturation pressure.

Vaporization and condensation processes are strongly affected by a variety of factors, including fluid velocities (Reynolds number), vaporization temperature (changed by the BPE), streams' physical properties, and geometrical equipment features (*e.g.*, tube pattern arrangement, and external and internal tube diameters) (Abraham and Mani, 2015). Additional information about the effects of these parameters on the optimal MEE-MVR system configuration and operational conditions are presented in Onishi et al.

(2017a). Since horizontal-tube falling film arrangements presents higher heat transfer coefficients than vertical ones, these type of configuration exhibits reduced equipment size and, therefore, lower capital investment (Qiu et al., 2015).

Flashing tanks are placed between evaporation effects to recover energy from condensate vapor (or distillate) by reducing its pressure (and temperature). Hence, this type of equipment allows improving the system energy performance through heat integration. As the flashed off condensate vapor in an *i*-effect is added together with the vapor from the boiling process to the next effect, both streams should present the same pressure. In spite of pressure equality, these streams can be at different temperatures. So, mixers should be included in the superstructure. As aforementioned, energy and economic analyses performed in our previous work (Onishi et al., 2017b) have revealed that MEE systems with single-stage compression are generally more cost-effective (freshwater production cost of 6.70 US$ per cubic meter with 2.78 US$ of electric power consumed per freshwater cubic meter) than multistage compression ones for the ZLD desalination of shale gas flowback water. This result is mainly due to the capital cost related to the equipment acquisition and the cooling expenses required by intercooling multistage compressors. For this reason, a single-stage mechanical vapor compressor driven by electricity is used to operate on closed vapor recompression cycle. Consequently, all vapor generated in the system (by feed evaporation and flash separation) is superheated via compression to meet evaporation energy requirements.

Due to the electric-driven compressor, the MEE-MVR system does not need other energy sources. However, we consider steam as an additional energy supply for the desalination system to avoid oversized equipment. As above-mentioned, equipment capacities are scenario independent decision variables. Therefore, process optimization for obtaining a system able to operate in a large range of feeding scenarios can lead to worst case sizing solutions. In other words, the equipment should be large enough to deal with extreme feeding conditions. As there is an optimal trade-off between the equipment size (capital cost) and energy consumption (operational expenses), it is clearly possible to reduce the equipment capacity by providing an external energy source. Finally, the MEE-MVR system also contains a shell-and-tube heat exchanger used to preheat the shale gas flowback water (henceforth referred as feed water), by taking advantage of sensible energy from condensed vapor. Obviously, this equipment promotes further heat transfer enhancement of the ZLD system. Moreover, feed preheating is essential to maintain the process productivity throughout annual climate changes.

A backward feeding configuration is admitted, so that preheated water is introduced in the last evaporator effect *i*, whereas brine (from previous effects) is added as feed water to the effects 1 to (*i*-1). As a consequence of the backward configuration, brine should flow from the last effect towards the first one. However, vapor generated in the effects and flashed off vapor is conducted towards the last evaporation effect, where it is sent to the compressor to be used as energy source to drive the ZLD system. Because vapor streams follow the temperature and pressure drop direction, the last effect should depict the lowest values for these variables. Given that vapor pressure is monotonically decreased throughout the evaporator, pumps units should be allocated between successive effects to permit brine transportation. Further information on shale gas flowback water desalination by MEE-MVR systems can be found in references (Onishi et al., 2017a; 2017b).

The multiscenario stochastic NLP-based model for the optimal MEE-MVR system design is developed in the following sections.

4. Stochastic multiscenario model

The stochastic multiscenario model is based on our previous deterministic NLP-based approaches presented in Onishi et al. (2017a; 2017b). In general, the stochastic NLP model is developed by modifying such deterministic mathematical formulations to account for distinct feeding scenarios. Nevertheless, significant improvements on the process are considered in this new approach. Firstly, we consider an extra external energy source (*i.e.*, steam) to avoid oversized equipment. Additionally, a new function is included in the optimization model, for describing the distribution of the compressor isentropic efficiency in the search space *s*. The consideration of the variable efficiency in the different scenarios allows obtaining a more precise and robust operating performance for the MEE-MVR desalination system.

The stochastic multiscenario model includes the modelling equations for the design of all equipment used in the MEE-MVR system (which encompasses the multiple-effect horizontal-tube evaporator, flashing tanks, mechanical vapor compressor and feeding preheater). More precisely, the modelling formulation comprises equipment sizing equations, mass and energy balances, constraints on temperature, and temperature and pressure feasibilities. We emphasize that the latter equations should explicitly consider the effect of the uncertain well parameters (feed water flowrate and salinity). Without exception, all equipment sizing-related equations remain unaffected by this source of uncertainty.

As above-mentioned, the decision variables are classified as scenario-dependent and scenario independent. The first group includes streams mass flowrates, salinities, temperatures, pressures, thermodynamic properties, and operational performance variables (*e.g.*, heat requirements and compression work). On the other hand, the scenario independent variables comprise all equipment capacities (*e.g.*, heat transfer areas and volumes). Note that well data uncertainty also affects the objective function. In this case, the minimization of the expected total annualized cost is considered to optimize the problem. We consider the following assumptions to simplify the multiscenario NLP model:

- *(i)* Steady state operation.
- *(ii)* Thermal losses can be disregarded in the feeding preheater and single-stage mechanical vapor compressor.
- *(iii)* Pressure drop in horizontal falling film tubes can be negligible.
- *(iv)* Temperature and pressure drops can be neglected in the demister.
- *(v)* Starter power can be neglected for the mechanical vapor compressor.
- *(vi)* Non-equilibrium allowance (NEA) can be neglected in the evaporator.
- *(vii)* Vapor streams from evaporation effects behave as ideal gases.
- *(viii)* Condensate product (freshwater) can be obtained with zero salinity.
- *(ix)* Mechanical vapor recompression cycle is modelled by an isentropic process.
- *(x)* Capital investment in mixers and pumps can be negligible for cost estimations.

The following sets are defined for improved development of the stochastic multiscenario NLP-based model:

$$I = \left\{ i \,/\, i = 1, 2, ..., I \ \text{ is an evaporation effect} \right\}$$
$$S = \left\{ s \,/\, s = 1, 2, ..., S \ \text{ is a feeding scenario} \right\}$$

The modelling equations for all equipment considered in the MEE-MVR system are presented in next sections.

4.1. Design of the multiple-effect evaporator

4.1.1. Mass balances

The mass balances in each evaporator effect *i* for each feeding scenario *s* are given by the following equations.

$$\dot{m}_{i+1,s}^{brine} = \dot{m}_{i,s}^{brine} + \dot{m}_{i,s}^{vapor} \qquad \forall 1 \le i \le I-1,\ \forall s \in S \tag{1}$$

$$\dot{m}_{i+1,s}^{brine} \cdot S_{i+1,s}^{brine} = \dot{m}_{i,s}^{brine} \cdot S_{i,s}^{brine} \qquad \forall 1 \le i \le I-1,\ \forall s \in S \tag{2}$$

In the first evaporation effect, the brine salinity should be equal to its outlet design specification to achieve the ZLD condition. For evaporation effects 1 to *I*-1, brine from subsequent effects is added as feed water (as a result of the backward feeding configuration); whereas in last effect *I*, the feeding stream corresponds to the feed water (*i.e.*, shale gas flowback water). The mass balances for the last effect *I* are given by **Eq. (3)** and **Eq. (4)**.

$$\tilde{m}_{in,s}^{feed} = \dot{m}_{i,s}^{brine} + \dot{m}_{i,s}^{vapor} \qquad \forall i = I,\ \forall s \in S \tag{3}$$

$$\tilde{m}_{in,s}^{feed} \cdot \tilde{S}_{in,s}^{feed} = \dot{m}_{i,s}^{brine} \cdot S_{i,s}^{brine} \qquad \forall i = I,\ \forall s \in S \tag{4}$$

In which, $\tilde{m}_{in,s}^{feed}$ and $\tilde{S}_{in,s}^{feed}$ are the stochastic parameters that define flowrate and salinity for the feed water in the set of distinct scenarios.

4.1.2. Global energy balances

Global energy balances in each evaporation effect *i* are performed for all feeding scenarios. The global energy balance in the effect *i* and scenario *s* should include inlet heat flows from condensed vapor and feed water, and brine and saturated vapor energy outflows. The global energy balances in each evaporation effect *i* and scenario *s* are given by **Eq. (5)** and **Eq. (6)**.

$$Q_{i,s} + \dot{m}_{i+1,s}^{brine} \cdot H_{i+1,s}^{brine} = \dot{m}_{i,s}^{brine} \cdot H_{i,s}^{brine} + \dot{m}_{i,s}^{vapor} \cdot H_{i,s}^{vapor} \qquad \forall i < I,\ \forall s \in S \tag{5}$$

$$Q_{i,s} + \tilde{m}_{in,s}^{feed} \cdot H_{i,s}^{feed} = \dot{m}_{i,s}^{brine} \cdot H_{i,s}^{brine} + \dot{m}_{i,s}^{vapor} \cdot H_{i,s}^{vapor} \qquad \forall i = I,\ \forall s \in S \tag{6}$$

In which, $Q_{i,s}$ is the heat flow added to the system boundary by the condensed vapor. The specific enthalpies for the brine ($H_{i,s}^{brine}$), boiling vapor ($H_{i,s}^{vapor}$) and feeding water ($H_{i,s}^{feed}$) are estimated by correlations exhibited in **Appendix A**. It should be noted that vapor and brine streams in an effect *i* and scenario *s* are considered to be at the same boiling temperature $T_{i,s}^{boiling}$.

4.1.3. Boiling temperature

The temperature in each evaporation effect *i* and scenario *s* is estimated by **Eq. (7)**, considering the effect of the boiling point elevation $BPE_{i,s}$ on its ideal temperature.

$$T_{i,s}^{boiling} = T_{i,s}^{ideal} + BPE_{i,s} \qquad \forall i \in I,\ \forall s \in S \tag{7}$$

The correlation for the estimation of the boiling point elevation $BPE_{i,s}$ in the evaporation effect *i* and scenario *s* is presented in **Appendix A**.

4.1.4. Heat requirements

In the first effect of the evaporator, the energy requirements should comprise the latent heat for the superheated vapor condensation, in addition to the sensible heat to achieve outlet condensate temperature. For remaining effects, latent heat of vaporization is added to the system by the flashed off condensate vapor and boiling vapor from previous effects. Heat flows in an evaporation effect *i* and scenario *s* are calculated by the following equations.

$$Q_{i,s} = \dot{m}_s^{sup} \cdot Cp_{i,s}^{vapor} \cdot \left(T_s^{sup} - T_{i,s}^{condensate}\right) + \dot{m}_s^{sup} \cdot \left(H_{i,s}^{cv} - H_{i,s}^{condensate}\right) \ + \ Q_s^{external} \qquad \forall i = 1,\ \forall s \in S \tag{8}$$

$$Q_{i,s} = \left(\dot{m}_{i-1,s}^{vapor} + \dot{m}_{c_{i-1,s}}^{vapor}\right) \cdot \lambda_{i,s} \qquad \forall i > 1,\ \forall s \in S \tag{9}$$

In **Eq. (8)**, the term $Q_s^{external}$ indicates the energy amount from the external source (steam) used to avoid oversized equipment:

$$Q_s^{external} = \dot{m}_s^{steam} \cdot Cp_s^{vapor} \cdot \left(T_s^{steam} - T_{i,s}^{condensate}\right) + \dot{m}_s^{steam} \cdot \left(H_{i,s}^{cv} - H_{i,s}^{condensate}\right) \qquad \forall i = 1,\ \forall s \in S \tag{10}$$

Also in **Eq. (8)**, T_s^{sup} and $T_{i,s}^{condensate}$ indicate the temperatures for the superheated vapor and condensate, respectively. $T_{i,s}^{condensate}$ is obtained by setting the vapor pressure at the compressor outlet (P_s^{sup}) in the Antoine Equation (see **Appendix A**). In addition, the specific enthalpies for vapor ($H_{i,s}^{cv}$) and liquid ($H_{i,s}^{condensate}$) phases of the condensate are estimated by correlations as shown in **Appendix A**. In **Eq. (9)**, $\lambda_{i,s}$ represents the vaporization latent heat, while $\dot{m}_s^{sup}$ indicates the mass flowrate of the superheated vapor calculated according to **Eq. (11)**.

$$\dot{m}_s^{sup} = \dot{m}_{i,s}^{vapor} + \dot{m}_{c_{i,s}}^{vapor} \qquad \forall i = I,\ \forall s \in S \tag{11}$$

In which, $\dot{m}_{i,s}^{vapor}$ and $\dot{m}_{c_{i,s}}^{vapor}$ are the boiling and flashed off vapor mass flowrates from the condensate, respectively.

4.1.5. Heat transfer area

The total heat transfer area of the evaporator ($A^{evaporator}$) is expressed by **Eq. (12)** as the sum of the areas of each evaporation effect *i*. Note that the evaporator heat transfer area should be adequate for the flowback water desalination in all distinct feeding scenarios set. For this reason, we consider this variable as scenario independent.

$$A^{evaporator} = \sum_{i=1}^{I} A_i \tag{12}$$

In the first evaporation effect, the area of heat transfer should be given by the sum of the areas related to the sensible and latent heat transfer, respectively:

$$A_i \geq \begin{bmatrix} \dot{m}_s^{sup} \cdot Cp_{i,s}^{vapor} \cdot \left(T_s^{sup} - T_{i,s}^{condensate}\right) \Big/ \left(U^S \cdot LMTD_{i,s}\right) \\ + \dot{m}_s^{sup} \cdot \left(H_{i,s}^{cv} - H_{i,s}^{condensate}\right) \Big/ U_{i,s} \cdot \left(T_{i,s}^{condensate} - T_{i,s}^{boiling}\right) \end{bmatrix} \quad \forall i = 1,\ \forall s \in S \tag{13}$$

In which, U^S is a known parameter that indicates the overall heat transfer coefficient for the estimation of the sensible heat transfer area. $H_{i,s}^{cv}$ and $H_{i,s}^{condensate}$ are the specific enthalpies for the condensate vapor and liquid phases (both estimated at temperature of condensation $T_{i,s}^{condensate}$), respectively (see **Appendix A**). For the evaporation effects 2 to *I*, the heat transfer area is calculated as follows:

$$A_i \geq Q_{i,s} \Big/ \left(U_{i,s} \cdot LMTD_{i,s}\right) \qquad \forall i > 1,\ \forall s \in S \tag{14}$$

In which, $Q_{i,s}$ indicates the heat requirements in the evaporation effect *i* and scenario *s* determined by **Eq. (9)**. The overall heat transfer coefficient $U_{i,s}$ is obtained using the correlation proposed by Al-Mutaz and Wazeer (2014):

$$U_{i,s} = 0.001 \cdot \begin{bmatrix} 1939.4 + 1.40562 \cdot \left(T_{i,s}^{boiling}\right) \\ -0.00207525 \cdot \left(T_{i,s}^{boiling}\right)^2 + 0.0023186 \cdot \left(T_{i,s}^{boiling}\right)^3 \end{bmatrix} \quad \forall i > 1,\ \forall s \in S \tag{15}$$

The log mean temperature difference $LMTD_{i,s}$ in each evaporation effect *i* and scenario *s* is calculated by the Chen's approximation (Chen, 1987), to avoid numeral difficulties for matching temperature differences:

$$LMTD_{i,s} = \left[0.5 \cdot \left(\theta_{1i,s} \cdot \theta_{2i,s}\right) \cdot \left(\theta_{1i,s} + \theta_{2i,s}\right)\right]^{\frac{1}{3}} \quad \forall i \in I,\ \forall s \in S \tag{16}$$

The temperatures differences $\theta_{1i,s}$ and $\theta_{2i,s}$ are estimated by **Eq. (17)**.

$$\theta_{1i,s} = \begin{cases} T_{s}^{sup} - T_{i,s}^{boiling} & \forall i = 1,\ \forall s \in S \\ T_{i,s}^{sat} - T_{i,s}^{boiling} & \forall i > 1,\ \forall s \in S \end{cases} \quad \text{and} \quad \theta_{2i,s} = \begin{cases} T_{i,s}^{condensate} - T_{i+1,s}^{boiling} & \forall i = 1,\ \forall s \in S \\ T_{i,s}^{sat} - T_{i+1,s}^{boiling} & \forall 1 < i < I,\ \forall s \in S \\ T_{i,s}^{sat} - T_{i,s}^{feed} & \forall i = I,\ \forall s \in S \end{cases} \tag{17}$$

For avoiding non-uniform area distribution throughout the evaporation effects, the following constraints are added to the model.

$$A_i \le n \cdot A_{i-1} \quad \forall i > 1 \tag{18}$$

$$A_i \ge A_{i-1} \quad \forall i > 1 \tag{19}$$

The model is solved by setting the parameter *n* equal to 3. Nonetheless, the parameter *n* can be chosen arbitrarily in accordance with the designer preferences. Evidently, these constraints can be easily removed from the mathematical model.

4.1.6. Pressure feasibility

The vapor pressure $P_{i,s}^{vapor}$ should be monotonically decreased throughout the distinct evaporation effects. Surely, this pressure feasibility should be ensured for all feeding scenarios.

$$P_{i,s}^{vapor} \ge P_{i+1,s}^{vapor} + \Delta P_{\min} \quad \forall i < I,\ \forall s \in S \tag{20}$$

For avoiding equipment instability, the vapor pressure $P_{i,s}^{vapor}$ in an evaporation effect *i* and scenario *s* should match the pressure of saturated vapor from the subsequent effect.

$$P_{i,s}^{vapor} = P_{i+1,s}^{sat} \qquad \forall i < I,\ \forall s \in S \tag{21}$$

4.1.7. Constraints on temperature

Constraints on temperature should be included in the model to avoid temperature crossovers in each evaporator effect *i* and scenario *s*. These temperature constraints are expressed by **Eq. (22) – Eq. (29)**.

$$T_s^{sup} \geq T_{i,s}^{condensate} + \Delta T_{\min}^1 \qquad \forall i = 1,\ \forall s \in S \tag{22}$$

$$T_{i-1,s}^{boiling} \geq T_{i,s}^{condensate} + \Delta T_{\min}^1 \qquad \forall i > 1,\ \forall s \in S \tag{23}$$

$$T_{i,s}^{boiling} \geq T_{i+1,s}^{boiling} + \Delta T_{\min}^2 \qquad \forall i < I,\ \forall s \in S \tag{24}$$

$$T_{i,s}^{boiling} \geq T_{i,s}^{feed} + \Delta T_{\min}^2 \qquad \forall i = I,\ \forall s \in S \tag{25}$$

$$T_{i,s}^{condensate} \geq T_{i+1,s}^{boiling} + \Delta T_{\min}^3 \qquad \forall i < I,\ \forall s \in S \tag{26}$$

$$T_{i,s}^{condensate} \geq T_{i,s}^{feed} + \Delta T_{\min}^3 \qquad \forall i = I,\ \forall s \in S \tag{27}$$

$$T_{i,s}^{condensate} \geq T_{i,s}^{boiling} + \Delta T_{\min}^4 \qquad \forall i \in I,\ \forall s \in S \tag{28}$$

$$T_{i,s}^{sat} \geq T_{i,s}^{boiling} + \Delta T_{\min}^4 \qquad \forall i \in I,\ \forall s \in S \tag{29}$$

4.2. Design of flashing tank separators

4.2.1. Mass balances

The mass balances in the flashing tank *i* in each scenario *s* are given by **Eq. (30)** and **Eq. (31)**.

$$\dot{m}_{s}^{sup} = \dot{m}_{c_{i,s}}^{vapor} + \dot{m}_{c_{i,s}}^{liquid} \qquad \forall i = 1,\ \forall s \in S \tag{30}$$

$$\dot{m}_{i-1,s}^{vapor} + \dot{m}_{c_{i-1,s}}^{vapor} + \dot{m}_{c_{i-1,s}}^{liquid} = \dot{m}_{c_{i,s}}^{vapor} + \dot{m}_{c_{i,s}}^{liquid} \qquad \forall i > 1,\ \forall s \in S \tag{31}$$

In which, $\dot{m}_{c_{i,s}}^{vapor}$ and $\dot{m}_{c_{i,s}}^{liquid}$ indicate the flashed off mass flowrates of the condensate vapor and liquid phases, respectively.

4.2.2. Global energy balances

Global energy balances in each flashing tank *i* and scenario *s* are stated by the following equations.

$$\dot{m}_{s}^{sup} \cdot H_{i,s}^{condensate} = \dot{m}_{c_{i,s}}^{vapor} \cdot H_{c_{i,s}}^{vapor} + \dot{m}_{c_{i,s}}^{liquid} \cdot H_{c_{i,s}}^{liquid} \qquad \forall i = 1,\ \forall s \in S \tag{32}$$

$$\left(\dot{m}_{i-1,s}^{vapor} + \dot{m}_{c_{i-1,s}}^{vapor}\right) \cdot H_{i,s}^{condensate} + \dot{m}_{c_{i-1,s}}^{liquid} \cdot H_{c_{i-1,s}}^{liquid} = \dot{m}_{c_{i,s}}^{vapor} \cdot H_{c_{i,s}}^{vapor} + \dot{m}_{c_{i,s}}^{liquid} \cdot H_{c_{i,s}}^{liquid} \qquad \forall i > 1,\ \forall s \in S \tag{33}$$

In which, $H_{i,s}^{condensate}$ and $H_{c_{i,s}}^{liquid}$ correspond to the specific enthalpy for liquid estimated at the condensate temperature ($T_{i,s}^{condensate}$) and ideal temperature ($T_{i,s}^{ideal}$), correspondingly. $H_{c_{i,s}}^{vapor}$ is the specific enthalpy for the vapor at the same ideal temperature ($T_{i,s}^{ideal}$). It should be highlighted that, for the estimations of liquid specific enthalpy of the condensate, salt mass fraction $X_{i,s}^{salt}$ must be considered equal to zero. The correlations to estimate liquid and vapor specific enthalpies are shown in **Appendix A**.

4.2.3. Flashing tank volume

The volume of each flashing tank separator *i* is calculated by **Eq. (34)** and **Eq. (35)**. Clearly, the flashing tank should be able to simultaneously deal with all distinct feeding scenarios. Thus, this variable should be considered as scenario independent.

$$V_i^{flash} \geq \left(\dot{m}_s^{sup} \cdot t\right) / \rho_{i,s} \qquad \forall i = 1,\ \forall s \in S \tag{34}$$

$$V_i^{flash} \geq \left(\dot{m}_{i-1,s}^{vapor} + \dot{m}_{c_{i-1,s}}^{liquid}\right) \cdot t / \rho_{i,s} \qquad \forall i > 1,\ \forall s \in S \tag{35}$$

In which, t indicates the retention time and $\rho_{i,s}$ represents the condensate density. In this approach, we consider the time of retention in the flashing tank as a parameter equal to 5 min. Correlations for estimating density, as well as all fluid physical properties in an effect *i* and scenario *s* are presented in **Appendix A**.

4.3. Design of the mechanical vapor compressor

4.3.1. Isentropic temperature

The isentropic temperature at the outlet of the mechanical compressor is calculated by the following equation.

$$T_s^{is} = \left(T_{i,s}^{mix} + 273.15\right) \cdot \left(P_s^{sup} / P_{i,s}^{vapor}\right)^{\frac{\gamma-1}{\gamma}} - 273.15 \qquad \forall i = I,\ \forall s \in S \tag{36}$$

In which, $T_{i,s}^{mix}$ is the mixture temperature calculated by an energy balance around the mixer in the last evaporation effect *I* and scenario *s*. γ corresponds to the heat capacity ratio parameter, and $P_{i,s}^{vapor}$ indicates the vapor pressure from the last evaporation effect *I* for the same scenario *s*. Observe that the pressure of the superheated vapor P_s^{sup} should be constrained by a maximum compression ratio $CR_{\max}$ as stated by the following equation.

$$P_s^{sup} \le CR_{\max} \cdot P_{i,s}^{vapor} \qquad \forall i = I \;,\; \forall s \in S \tag{37}$$

4.3.2. Superheated vapor temperature

The superheated vapor temperature from the mechanical compressor in each scenario *s* is determined by **Eq. (38)**.

$$T_s^{sup} = T_{i,s}^{mix} + \frac{1}{\eta_s} \cdot \left(T_s^{is} - T_{i,s}^{mix} \right) \qquad \forall i = I,\; \forall s \in S \tag{38}$$

In which, η_s is the isentropic efficiency of the compressor estimated for each feeding scenario *s* according to the next equation.

$$\eta_s = \left(0.35/0.8 \right) \cdot \left(W_s / WC - 0.2 \right) \;+\; 0.5 \qquad \forall s \in S \tag{39}$$

In which, W_s is the compression work performed in the scenario *s*, while WC indicates the higher value (worst case) obtained for the compressor capacity:

$$WC \geq W_s \quad \forall s \in S \tag{40}$$

The **Eq. (39)** is valid for $0.5 \leq \eta_s \leq 0.85$ and $0.2 \leq W_s / WC \leq 1$. These constraints imply that the work performed by the compressor (W_s) in a scenario *s* should be restricted between 20% (with $\eta_s = 50\%$) to 100% (with $\eta_s = 85\%$) of the nominal capacity of the equipment (indicated by WC). Note that the scenario-dependent variable W_s should be calculated to determine the distributions of energy consumption by the compressor and its corresponding operational expenses; whereas WC should be used to estimate the capital investment in the compressor.

4.3.3. Compression work

The compression work performed by the mechanical vapor compressor in each scenario *s* is calculated by the following equation.

$$W_s = \dot{m}_s^{sup} \cdot \left(H_s^{sup} - H_{i,s}^{vapor} \right) \qquad \forall i = I,\ \forall s \in S \tag{41}$$

In which, H_s^{sup} and $H_{i,s}^{vapor}$ indicate vapor specific enthalpies that should be estimated at superheated vapor temperature (T_s^{sup}) and mixture temperature ($T_{i,s}^{mix}$) from last evaporation effect, respectively. The correlations for these estimations are presented in **Appendix A**.

4.3.4. Constraints on temperature and pressure

Constraints on the temperature and pressure at the compressor outlet should be used to ensure the proper functioning of this equipment.

$$T_s^{sup} \geq T_{i,s}^{mix} \qquad \forall i = I,\ \forall s \in S \tag{42}$$

$$P_s^{sup} \geq P_{i,s}^{vapor} \qquad \forall i = I,\ \forall s \in S \tag{43}$$

4.4. Design of the feeding preheater

4.4.1. Global energy balance

The global energy balance in the feeding preheater is stated by **Eq. (44)**.

$$\dot{m}_{c_{i,s}}^{liquid} \cdot Cp_{i,s}^{condensate} \cdot \left(T_{i,s}^{ideal} - T_{out,s}^{freshwater}\right) = \tilde{m}_{in,s}^{feed} \cdot Cp_{in,s}^{feed} \cdot \left(T_{i,s}^{feed} - T_{in,s}^{feed}\right) \qquad \forall i = I,\ \forall s \in S \tag{44}$$

In which, $T_{out,s}^{freshwater}$ represents the temperature of the produced freshwater in each scenario *s*, while $T_{in,s}^{feed}$ indicates the feeding temperature (shale gas flowback water). The liquid specific heats of the condensate ($Cp_{i,s}^{condensate}$) and feed water ($Cp_{in,s}^{feed}$) are estimated by correlations shown in **Appendix A**.

4.4.2. Heat transfer area

The heat transfer area of the feeding preheater $A^{preheater}$ is calculated by the **Eq. (45)**. Again, the heat transfer area should be considered as a scenario independent variable to guarantee the suitability of this equipment under different feeding conditions (defined by the scenarios set).

$$A^{preheater} \geq \dot{m}_{c_{i,s}}^{liquid} \cdot Cp_{i,s}^{condensate} \cdot \left(T_{i,s}^{ideal} - T_{out,s}^{freshwater}\right) \Big/ \left(U_s \cdot LMTD_s\right) \qquad \forall i = I,\ \forall s \in S \qquad (45)$$

In which, U_s is the overall heat transfer coefficient estimated by **Eq. (15)**, considering the ideal temperature $T_{i,s}^{ideal}$. The logarithmic mean temperature difference $LMTD_s$ in the preheater is calculated by **Eq. (16)**, by considering:

$$\theta_{1s} = T_{i,s}^{ideal} - T_{i,s}^{feed} \quad \forall i = I,\ \forall s \in S \quad \text{and} \quad \theta_{2s} = T_{out,s}^{freshwater} - T_{in,s}^{feed} \quad \forall s \in S \qquad (46)$$

4.5. Design specification for Zero-Liquid Discharge

The MEE-MVR system is designed to operate under ZLD condition. For this objective, the brine salinity in the first evaporation effect should achieve its specification of design. ZLD operation is ensured by the following constraint.

$$S_{i,s}^{brine} \geq S^{design} \qquad \forall i = 1,\ \forall s \in S \qquad (47)$$

It should be emphasized that the inclusion of this constraint in the model restricts the search space to solutions that meet a minimum salinity requirement S^{design} for the brine (*e.g.*, brine salinity near salt saturation conditions). Obviously, lower costs are expected for lesser brine salinity restrictions.

4.6. Stochastic objective function

The multiscenario stochastic model is optimized to obtain robust solutions, through the expected value minimization of the objective distribution represented by the total annualized cost. The stochastic objective function for minimization of the expected total annualized cost $TAC^{Expected}$ of the MEE-MVR system can be expressed as follows:

$$\begin{aligned}
&\min \quad TAC^{Expected} = \sum_{s=1}^{S} prob_s \cdot TAC_s = \sum_{s=1}^{S} prob_s \cdot \left(CAPEX + OPEX_s \right) \\
&s.t. \quad \text{Eq.(1) – Eq.(46)} \\
&\qquad S_{1,s}^{brine} \geq S^{design}
\end{aligned} \tag{48}$$

In which $prob_s$ represents the probability related to the occurrence of a specific scenario *s*, and TAC_s is the total annualized cost of the desalination system in this same scenario. In this work, we consider equal probabilities of occurrence for all feeding water scenarios. The total annualized cost distribution accounts for the capital investment in all equipment ($CAPEX$) used in the MEE-MVR system, and operational expenses in each scenario *s* ($OPEX_s$) related to the external steam source and electricity. Observe that the capital investment is a scenario independent variable. On the other hand, operating expenses should be defined by a stochastic function to capture all variability of the system's energy consumption in the uncertain search space. This is because a different system performance is obtained for each scenario *s*, while the equipment capacities should be the same for all scenarios. The distributions of capital investment and operational costs are given by **Eq. (49)** and **Eq. (50)**, respectively.

$$CAPEX = fac \cdot \left(\frac{CEPCI^{2015}}{CEPCI^{2003}} \right) \cdot \left[\begin{array}{l} \left(C_{PO} \cdot F_{BM} \cdot F_P \right)^{evaporator} + \left(C_{PO} \cdot F_{BM} \cdot F_P \right)^{compressor} + \\ \left(\sum_{i=1}^{I} C_{POi} \cdot F_{BM} \cdot F_P \right)^{flash} + \left(C_{PO} \cdot F_{BM} \cdot F_P \right)^{preheater} \end{array} \right] \tag{49}$$

$$OPEX_s = C^{electricity} \cdot W_s + C^{steam} \cdot Q_s^{external} \tag{50}$$

The annualization factor for the capital investment fac is calculated by the following equation (Smith, 2005):

$$fac = \left[(1 + fi)^{y} - 1 \right]^{-1} \cdot (1 + fi)^{y} \cdot fi \tag{51}$$

In which, fi expresses the fractional interest rate per year in an amortization period y. In **Eq. (49)**, C_{PO} indicates the unitary equipment cost (in kUS$) calculated by correlations presented in Turton et al. (2012) (flashing tank separators and feeding preheater), and in Couper et al. (2010) (evaporator and mechanical vapor compressor). F_{BM} is the correction factor for the unitary equipment cost that correlates the operational conditions to the materials of construction. In addition, the capital investment should be corrected for the appropriate year with the CEPCI index (Chemical Engineering Plant Cost Index). In **Eq. (50)**, $C^{electricity}$ and C^{steam} represent the parameters for the cost of electricity and steam energy services, respectively.

5. Scenario generation: probability function and sampling technique

In this section, we focus our attention on the generation of scenarios to properly describe the uncertainty associated with the well data. Our stochastic modelling approach is based on the assumption that the uncertain parameters (*i.e.*, feed water flowrate and salinity) can follow normal (Gaussian) correlated distributions. Thus, the uncertain parameters are modelled through a probability multivariate distribution for which random values (restricted by the distribution boundaries) are generated via Monte Carlo sampling technique. As result, the uncertain parameters are depicted by a set of representative scenarios with known probability of occurrence. As aforementioned, we assume the same probability of occurrence for all feeding scenarios. Note that a given scenario corresponds to a single sample of the uncertain parameters distribution (assumed as multivariate normal). These explicit scenarios together with their associated probabilities are used as input data for solving the optimization multiscenario model. Basically, our stochastic approach admits the calculation of all scenario-dependent variables for each value assumed by the random parameters, allowing constructing the total annualized cost distribution.

Correlated scenarios are generated from a multivariate normal distribution via a random number generator algorithm implemented in MATLAB based on the Mersenne twister algorithm proposed by Matsumoto and Nishimura (1998). The probability density function for correlated continuous random variables $X_1, X_2, \ldots, X_d$, where each variable has a univariate (or marginal) normal distribution is given by:

$$f_X(X_1, X_2, \ldots, X_d) = \frac{1}{\sqrt{(2\pi)^2 \mid \Sigma \mid}} \exp\left(-\tfrac{1}{2}(X-\mu)^T \Sigma^{-1}(X-\mu)\right) \tag{52}$$

In which, μ is a *d* dimensional vector with the expected value of each random variable (μ_i), Σ is a *d*×*d* covariance matrix, and $\left|\Sigma\right|$ is the determinant of Σ. The diagonal elements of Σ, which is a symmetric positive definite matrix, contain the variances for each variable (σ_i^2), while the off-diagonal elements of Σ contain the covariances between variables (σ_{ij}). It is worth to mention that a diagonal covariance matrix (*i.e.*, all covariances between variables are zero) implies that the random variables are not correlated. The scenario generation method requires the attribution of the expected values (nominal) and its variance for the uncertain parameters, in addition to their covariance matrix. The expected values considered for generating each representative distribution of uncertain parameters are shown in **Table 2**. The off-diagonal elements of the covariance matrix can be calculated from the correlation matrix ρ_{ij}. Both matrices are related as follows:

$$\rho_{ij} = \frac{\sigma_{ij}}{\sigma_i^2 \sigma_j^2} \tag{53}$$

Hence, a symmetric correlation matrix is defined to describe the interactions between the uncertain parameters. This symmetric matrix contains the information on each pair of correlated random variables, by setting all non-diagonal elements with a value between -1 and 1. It should be remarked that values ranging between -1 and 0 present negative correlation (which implies that one variable increases, while the other linearly decreases), whereas values ranging between 0 and 1 are positively correlated (which means that both variables linearly increase or decrease). If these factors assume values equal to zero, the uncertain pair of variables are uncorrelated (Sabio et al., 2014).

Based on real information from shale plays, we assume that the uncertain parameters have negative correlation. Typically, the salinity profile of the shale gas flowback water shows a significant increase when the flowrate is reduced in the first two weeks of well exploration (Acharya et al., 2011). The correlated feeding scenarios generated with normal multivariate distributions, by considering different matrix correlation factors are displayed in **Fig. S1** of the **supporting information**. Observe that the stochastic model is robust enough for dealing with scenarios generated by any sampling technique and/or correlation. Regarding the number of scenarios, the model accuracy generally increases as more scenarios are considered during the optimization.

Nevertheless, the CPU time to obtain a feasible solution is also increased due to computational limitations (see Law and Kelton (2000) for more information about how to obtain the best number of scenarios in stochastic programming models aimed at optimizing the expected value of an objective function distribution).

6. Results and discussion

An illustrative case study is performed to evaluate the accurateness of the proposed approach for synthesizing MEE-MVR desalination systems, under uncertainty of the shale gas flowback water data. **Fig. 1** depicts the superstructure proposed for the MEE-MVR desalination plant of the flowback water from shale gas production. Firstly, we present a comparison between the deterministic and stochastic solutions to emphasize the importance of considering the proposed stochastic approach to solve this type of problem. Then, we use the stochastic model to address the uncertainty related to the well data in the shale gas production. Finally, sensitivity analysis is carried out to assess the optimal system performance for distinct brine salinity conditions. The well data considered in this example are based on real information obtained from important shale plays in the U.S., including Barnett and Marcellus (Acharya et al., 2011; Haluszczak et al., 2013; Hayes, 2009; Jiang et al., 2013; Slutz et al., 2012; Thiel and Lienhard V, 2014; Vidic et al., 2013; Zammerilli et al., 2014) as shown in **Table 1**.

In this work, we consider expected mean (nominal) values of 8.68 kg s^{-1} (~750 m^3 day^{-1}) for the amount of shale gas flowback water—corresponding to the treating capacity of the MEE-MVR plant—and 80 g kg^{-1} (80k ppm) for the flowback water salinity. According to Slutz et al. (2012), the water amount required to complete each well—in horizontal drilling and hydraulic fracturing processes—is in a range of 12 700−19 000 m^3. However, this value can be very different for distinct wells (see **Table 1**). Thus, we assume an expected mean value of 15 000 m^3 for the amount of water required, and 25% for the injected fluid that returns to surface as flowback water—during the first 15 days from the beginning of well exploration—. In addition, we respect an annual scheduling that comprises the exploration of 20 wells divided in fracturing crews (maximum exploration of 3 wells at the same time) as proposed by Lira-Barragán et al. (2016). Consequently, about 11 250 m^3 of flowback water are recovered in the first 2 weeks of the shale gas production start (~750 m^3 day^{-1} or ~8.68 kg s^{-1}). Note that, if a standard deviation of 5% is considered from the mean value (15 000 m^3), then ~95% of the flowback water data will be between 13 500−16 500 m^3 (and ~99.7% between 12 750−17 250 m^3). In the same way, if standard deviations of 10% and 20% are considered, ~95% of the flowback water data can be found in ranges of 12 000−18 000 m^3 and 9 000−21 000 m^3, respectively. With this in mind, we consider that standard deviations of 5%, 10% and 20% are suitable to model the uncertainty associated with the amount of flowback water. However, higher standard deviations must be considered for the flowback water salinity due to the larger uncertainty related to these data (see **Table 1)**. Hence, if a standard deviation of 30% is considered from the expected mean value of the salt concentration in the flowback water (80k ppm); ~95% of the data will be in the range of 32−128k ppm. Nevertheless, it should be highlighted that the brine discharge salinity should be at least equal to 300 g kg^{-1} (300k ppm) to achieve ZLD operation (Han et al., 2017).

Additional data include the operational limitations on the ideal temperature and saturation pressure to prevent fouling and/or rusting problems in the evaporator (horizontal-tube falling film/nickel), which should be lower than 100 ºC and 200 kPa, correspondingly. A minimum temperature approach of 2 ºC is allowed for the superheated vapor and condensate streams, as well as for vapor and brine concentrate streams. Note that this minimum temperature approach is required to avoid temperature crossover in the effects of evaporation. Moreover, a minimum pressure and temperature drops between two successive effects are considered equal to 0.1 kPa and 0.1 ºC, respectively. The heat capacity ratio γ is considered to be equal to 1.33, while the maximum compression ratio $CR_{\max}$ is restricted to 3 for the mechanical compressor design (centrifugal/carbon steel). Cost data comprises the electricity—850.51 US$ (kW year)$^{-1}$—and steam—418.8 US$ (kW year)$^{-1}$—prices. An annualized cost factor (*fac*) of 0.16 is considered for capital cost estimations, which corresponds to an interest rate of 10% over an amortization period of 10 years. The problem data considered for the case study are summarized in **Table 2**.

6.1. Deterministic *vs* stochastic solution

Initially, we contrast the optimal solutions obtained from the deterministic and stochastic approaches for assessing the impact of uncertainty on the MEE-MVR system performance. Thus, we firstly solve the deterministic model through the minimization of the process total annualized cost. It should be highlighted that the deterministic model can be easily obtained from the proposed stochastic approach, by considering one single scenario. In this case, the optimization scenario should correspond to the expected mean (nominal) values for the well data (*i.e.*, 80 g kg^{-1} for the flowback water salinity and 8.68 kg s^{-1} for the flowrate). The deterministic model allows obtaining an optimal system configuration and corresponding operational conditions. Afterwards, equipment capacities obtained from this method—including evaporator and preheater heat transfers areas, flashing tanks volumes and compressor capacity—are fixed in the stochastic model to evaluate the system performance under distinct feeding scenarios.

The optimal MEE-MVR desalination system obtained by the deterministic approach is composed of two evaporator effects with heat transfers areas equal to 59.46

m^2 (7819.12 kW) and 178.36 m^2 (7674.59 kW), in addition to a mechanical vapor compressor with capacity of 457 kW ($\eta = 0.85$). Furthermore, a feed preheater with heat transfer area of 71.47 m^2 (1469.53 kW), and flashing tanks with volumes of 1.24 m^3 and 2.77 m^3 are also needed in the system. **Fig. 3** displays the optimal MEE-MVR system configuration and operational conditions obtained by the deterministic model. With this configuration, the system requires 177.21 kW of additional energy from the external steam source. The total annualized cost obtained for the deterministic case is equal to 1055 kUS\$ $year^{-1}$, comprising 463 kUS\$ $year^{-1}$ related to operational expenses (steam and electricity consumption) and 592 kUS\$ $year^{-1}$ associated with capital investment. It should be noted that the system operates at ZLD operation (salt concentration in the brine discharge equal to 300 g kg^{-1}). Under this condition, a freshwater production ratio of 6.37 kg s^{-1} is achieved by the desalination plant. This value corresponds to ~73.3% of condensate (freshwater) recovery. The freshwater production cost is equal to 5.25 US\$ per cubic meter (~0.02 US\$ $gallon^{-1}$), of which ~43% are related to energy consumption. Note that the cost of water disposal in Class II saline water injection sites (conventional deep-well injection) are between ~8−25 US\$ per cubic meter (~0.03−0.08 US\$ $gallon^{-1}$)—cost for water disposal in locally available wells in Barnett shale play—(Acharya et al., 2011). These values emphasize the economic viability of the proposed ZLD desalination system for the shale gas flowback water.

Hereafter, we perform the stochastic optimization by fixing the equipment capacities provided by the deterministic solution. In this case, feed data uncertainty is described via 100 different feeding scenarios generated by sampling technique. For this purpose, it is assumed a normal correlated distribution with 10% of standard deviation from the mean values (8.68 kg s^{-1} and 80 g kg^{-1}). In addition, we consider a correlation matrix factor of -0.8 (which means that the uncertain parameters are strongly correlated).

Observe that the number of scenarios is chosen as the smallest number of scenarios from which no significant differences is found between successive optimizations.

The stochastic solution obtained by considering the deterministic configuration presents an expected total annualized cost equal to 1129 kUS\$ year^{-1}. This amount corresponds to an increment of ~7% in comparison with the deterministic total annualized cost. It is emphasized that the total process cost is increased due to the adjustment of the operational conditions needed to enable the operation of the MEE-MVR system in all scenarios. Clearly, the MEE-MVR system has the same capital investment than the deterministic solution (592 kUS\$ year^{-1}). However, the operational expenses are different for each feeding scenario. For the first scenario, we report operational expenses of 286 kUS\$ year^{-1}, representing a decrease of ~38.2% in relation to the one obtained for the deterministic approach. In this scenario, the desalination system only requires 336.15 kW of electricity—which implies that the mechanical vapor compressor operates at 73.6% of the nominal equipment capacity with efficiency of $\eta = 0.73$—with no need for external steam.

Although some feeding scenarios present lower operating costs, more than 50% of them exhibit higher values than the one obtained in the deterministic solution. For instance, scenarios 49 and 66 show operational expenses equal to 479 kUS\$ year^{-1} and 572 kUS\$ year^{-1}, respectively. Even further increased values are obtained for scenarios 81 and 90 (705 kUS\$ year^{-1} and 803 kUS\$ year^{-1}, respectively). Note that the scenarios 49 and 66 consume 214.89 kW and 438.29 kW from the external energy source, correspondingly. Scenarios 81 and 90 use 755.27 kW and 988.97 of steam, respectively. Yet, the above-mentioned scenarios need the same amount of electricity (457 kW), which indicates that the compressor is working on its maximum nominal capacity. Scenario 100 presents the worst case for these expenses, presenting operational costs equal to 1386 kUS$ year^{-1}. This value represents an increase of ~200% in comparison with the deterministic solution. In the last scenario, energy consumption comprises 457 kW (with $\eta = 0.85$) of electricity and 2381.28 kW of steam. The operational expenses distribution in the uncertain search space is illustrated in **Fig. S2** of the **supporting information**. The energy consumption distribution throughout the distinct feeding scenarios is displayed in **Fig. 4**. We highlight that all scenarios operate at ZLD condition. For convenience, scenarios are sorted by ascending order of feed flowrate inlet data.

First and last scenarios show a similar freshwater production cost of ~6.8 US$ per cubic meter (~0.03 US$ gallon^{-1}), which corresponds to an increase of ~30% in comparison with the deterministic solution. **Fig. 5** depicts the freshwater cost distribution obtained via stochastic approach throughout the different feeding scenarios. For allowing comparisons with the deterministic solution, the freshwater production cost is estimated by considering the operating expenses and capital investment individually for each scenario. Therefore, energy consumption and respective operating expenses and freshwater production costs can be prohibitive for some feeding scenarios. This is due to the weak system performance under feeding conditions that have not been considered during its design task. For this reason, we stress the importance of the stochastic design to provide all system flexibility under process parameters variability. The stochastic MEE-MVR system design is shown in the following section.

6.2. Stochastic system design and risk analysis

For the stochastic optimization of the MEE-MVR system, we consider the previous expected mean values (8.68 kg s^{-1} and 80 g kg^{-1}), and standard deviations of 10% for both feed water flowrate and salt concentration. Again, feed data uncertainty is described via 100 distinct scenarios correlated by a matrix correlation factor of -0.8. The scenarios are sorted by ascending order of feed flowrate inlet data. **Fig. 6** shows the correlated feeding scenarios generated with a marginal normal multivariate distribution. In this case, the optimal MEE-MVR system obtained is composed of two evaporator effects with heat transfers areas of 66.31 m^2 and 198.93 m^2; in addition to a mechanical vapor compressor with capacity of 498.11 kW, and a feed preheater with heat transfer area of 72.62 m^2. Furthermore, two flashing tanks are also required in the system with volumes equal to 1.29 m^3 and 2.77 m^3, respectively. **Fig. 7** displays the optimal MEE-MVR system configuration obtained by the proposed stochastic model. Note that the total heat transfer area and compressor capacity are both increased by ~9%, in comparison with the optimal solution provided by the earlier deterministic approach. We emphasize that the equipment increment is needed to ensure the optimal system performance in all considered scenarios. The optimal solution for the MEE-MVR system presents an expected total annualized cost equal to 1110 kUS\$ $year^{-1}$, from which 637 kUS\$ $year^{-1}$ are related to the capital investment.

Distributions of energy consumption and corresponding operational expenses throughout the distinct feeding scenarios are displayed in **Fig. S3 and Fig. S4 of the supporting information**. In the latter distribution, the first scenario only consumes electricity (330.3 kW). For this reason, this scenario presents the lowest operating expenses (280.9 kUS\$ $year^{-1}$). However, other scenarios require energy consumption much more elevated than the first one. For example, the scenarios 81 and 90 need 498.11 kW (each one) of electricity; and, 366.52 kW and 541.71 kW of external steam, respectively. Consequently, these scenarios exhibit operational expenses equal to 577.14 kUS\$ $year^{-1}$ and 650.52 kUS\$ $year^{-1}$, correspondingly. It should be noted that the last scenario shows the highest energy consumption (1578.18 kW of steam and 498.11 of electricity) and related operating costs (1084.59 kUS\$ $year^{-1}$).

From scenario 45 onwards, the MEE-MVR system demands all maximum nominal capacity of the mechanical vapor compressor (498.11 kW). Moreover, the desalination system also starts consuming external steam from this scenario, as shown in **Fig. S3 (see supporting information)**. It is worth to mention that the desalination system obtained by the stochastic approach also achieves the ZLD condition in all considered scenarios. Though, the first scenario attains the lowest freshwater production ratio (4.08 kg s^{-1}). As expected, this scenario shows the highest freshwater production cost that is equal to 8.63 US$ per cubic meter (~0.033 US$ $gallon^{-1}$). On the other hand, the highest amount of produced freshwater is obtained by the last scenario (9.22 kg s^{-1}). For the latter, the freshwater cost is equal to 3.82 US$ per cubic meter (~0.015 US$ $gallon^{-1}$). Here, the freshwater production cost is estimated by means of the expected total annualized cost. **Fig. 8** displays the distributions for the freshwater production cost and produced freshwater throughout the distinct feeding scenarios.

Cumulative probability curves for the system economic performance (considering weakly and strongly correlated uncertain parameters) are depicted in **Fig. 9** and **Fig. 10**, respectively. In both cases, standard deviations of 5%, 10% and 20% from the expected mean values are considered for the generation of the uncertain scenarios. In these curves, the vertical axis indicates the probability of achieving an economic performance lesser or equal to a target value presented in the horizontal axis. For instance, if the decision-maker targets a maximum value for the process total annualized cost of 1200 kUS$ $year^{-1}$, **Fig. 9** shows that the 5% curve has ~97% of probability of achieving this goal; whereas the 10% and 20% curves present lower probabilities of ~90% and ~75%, respectively. If a more ambitious objective of 1100 kUS$ $year^{-1}$ is targeted for the economic performance, the probabilities are significantly reduced to ~88% (5% curve), ~68% (10% curve) and ~48% (20% curve).

If the uncertain parameters are strongly correlated as considered in **Fig. 10**, the probabilities of attaining the more conservative goal (1200 kUS\$ year^{-1}) are reduced for all standard deviations (5%, 10% and 20% curves). In this case, the probabilities are equal to ~96% (5% curve), ~87% (10% curve) and ~60% (20% curve), correspondingly. A thorough examination of both curves reveals that the consideration of uncertain parameters with higher standard deviations involves riskier decision-making. It should be noted that higher standard deviation curves show lower probability of reaching a certain economic performance. More precisely, the 20% curve in **Fig. 9** presents ~12% of probability of exceeding a target cost of 1311 kUS\$ year^{-1}, while this probability is null for the 5% curve.

Fig. 9 and **Fig. 10** also display the minimum and maximum values for the total annualized cost, as well as the expected economic performance obtained for all standards deviations. In **Fig. 9**, the expected total annualized cost is increased by ~7.9% between the optimal solutions found for 5% (1066 kUS\$ year^{-1}) and 20% (1150 kUS\$ year^{-1}) of standard deviations. For the 5% curve, the upper bound for the economic performance is ~35% higher than its corresponding minimum value. Instead, the 20% standard deviation curve presents ~181.3% of increase in the total annualized cost when its extreme solutions are compared. Thus, the solutions present worse expected economic performance, and more variability in the total annualized cost as the uncertainty level is increased during the system design. Note that in **Fig. 10**, the expected total annualized cost for the 20% standard deviation (1200 kUS\$ year^{-1}) is ~12% higher than the optimal solution obtained for 5% of standard deviation (1070 kUS\$ year^{-1}).

Finally, even worse expected performance and higher variability in the total annualized cost are verified as the correlation level is increased between the uncertain parameters. This is because the correlated parameters assume simultaneously the lowest and highest values of the uncertain search space, which leads to extreme scenarios. We report that other risk management metrics have been used to solve this problem, including the worst case for the total annualized cost and downside risk. In these cases, multi-objective optimizations have been performed through the minimization of the expected value and the referred metrics. However, the obtained Pareto curves did not exhibit significant trade-offs between solutions. Hence, variations in the upper bound (ε-constraint) for these risk metrics (worst case and downside risk) did not change the expected value for the total annualized cost.

The proposed NLP-based model for both deterministic and stochastic optimizations of the MEE-MVR desalination system has been implemented in GAMS (version 24.7.4), and optimized by the interior-point solver IPOPT (Wächter and Biegler, 2006) with CPLEX as sub-solver. A personal computer with an Intel Core i5-2520M 2.5 GHz processor and 8 GB RAM running Windows 10 has been used for solving all case studies. The CPU time for the deterministic optimization has not exceeded 1 s, while the stochastic ones have required 10 to 15 s to get optimal solutions. In the deterministic case, the mathematical model encompasses 93 continuous variables, 105 constraints with 292 Jacobian (non-zeros) elements, of which 106 are nonlinear. Instead, the stochastic mathematical model contains 7 320 continuous variables, 9 114 constraints with 26 131 Jacobian (non-zeros) elements, of which 10 303 are nonlinear.

6.3. Sensitivity analysis

A straightforward sensitivity analysis is carried out to evaluate the energy and economic performances of the MEE-MVR system under different discharge brine salinities. In this way, we consider several ZLD conditions defined by the brine salinity ranging between 200 and 320 g kg^{-1} 1 (200–320 k ppm). The stochastic optimizations are performed by considering the same expected mean values for inlet feed water salinity and flowrate (8.68 kg s^{-1} and 80 g kg^{-1}), as well as the same standard deviations (10%) and matrix correlation factor (-0.8) for the generation of the uncertain parameters. Once again, we consider an uncertain search space composed by 100 distinct feeding scenarios. Box and whisker plots for energy consumption and total annualized cost according to discharge brine salinity are displayed in **Fig. S5** and **Fig. S6 (supporting information)**, respectively. These plots indicate that the total energy consumption (related to electricity and steam) and total annualized cost (including capital investment and operational expenses) are more elevated as higher ZLD constraints are imposed on the system design. It should be highlighted that for the same inlet feed conditions given by the scenarios, higher restrictions on ZLD conditions imply greater brine concentrations.

The expected total energy consumption for the brine salinity of 200 g kg^{-1} is equal to 572 kW, whereas the ZLD constraint of 320 g kg^{-1} requires 657 kW of energy. This value represents an increase of ~15% in comparison with the first solution. In accordance with these results, expected total annualized cost is increased by ~21% between the brine salinity conditions of 200 g kg^{-1} (945 kUS$ $year^{-1}$) and 320 g kg^{-1} (1144 kUS$ $year^{-1}$). The distributions of energy consumption and total annualized cost are also shown in **Fig. S5** and **Fig. S6**. As can be observed in **Fig. S6**, 50% of the solutions for the system economic performance under brine salinity constraint of 250 g kg^{-1} are in the range of 945−1070 kUS$ $year^{-1}$ (quartiles 1 and 3). For this case, minimum and maximum values for the total annualized cost distribution are equal to 839 kUS$ $year^{-1}$ and 1571 kUS$ $year^{-1}$, respectively. The expected mean value for the total annualized cost is equal to 1029 kUS$ $year^{-}1$, while the median is 1005 kUS$ $year^{-1}$. It is important to emphasize that the proposed stochastic multiscenario approach, allows obtaining robust solutions when accounting for parameter uncertainty. Such system performance robustness cannot be ensured by a deterministic model, since it is not able to provide the distributions for the energy consumption and process costs.

7. Conclusions

A new stochastic optimization model for the design of ZLD desalination systems under uncertainty is introduced in this work. The model is based on a multistage superstructure defined by multiple-effect evaporation process with heat integration and mechanical vapor recompression (MEE-MVR). The MEE-MVR system is especially developed for the desalination of high-salinity flowback water from shale gas production. Our main goal is to enhance energy efficiency of the process through the reduction of brine discharges, while accounting for distinct water feeding scenarios. To achieve this objective, we define the outflow brine salinity near to salt saturation as a design constraint to reach ZLD operation. Important improvements in the process are implemented, including the use of an external energy source to avoid oversized equipment. Additionally, we consider the compressor isentropic efficiency as a variable throughout the different scenarios. This novelty allows obtaining a more precise and robust system operational performance. In this new approach, feed water (*i.e.*, shale gas flowback water) salinity and flowrate are both treated as uncertain design parameters. These uncertain parameters are mathematically modelled as a set of correlated scenarios with given probability of occurrence. The feeding scenarios are described by multivariate normal distribution generated via sampling technique with symmetric correlation matrix. The resulting stochastic multiscenario NLP-based model is optimized in GAMS, through the minimization of the expected total annualized cost.

An illustrative case study is performed to evaluate the capabilities of the proposed new approach for the design of MEE-MVR desalination systems under uncertainty of shale gas flowback water data. Firstly, we compare the optimal solutions obtained from the deterministic and stochastic models for assessing the impact of uncertainty on the energy and economic system performances. In this case, our results show that the energy consumption and corresponding operational expenses and freshwater production costs can be prohibitive for some scenarios. This is a result of the weak system performance under feeding water conditions that have not been accounted during the MEE-MVR design task. Therefore, it is clear that the stochastic design approach should be considered to provide system flexibility under variability of process uncertain parameters.

Afterwards, we carry out the stochastic optimization of the MEE-MVR desalination system. This is an innovative approach, since it allows obtaining the distributions of energy consumption and corresponding operational expenses throughout the distinct feeding scenarios. Still, we construct cumulative probability curves to appraise the financial risk associated with uncertain space for distinct standard deviations of mean values. A thorough inspection of these curves indicates that the consideration of uncertain parameters with higher standard deviations involves riskier decision-making. The latter can be explained by the lower probability of reaching a certain economic performance, as depicted by the curves with higher standard deviation.

Lastly, a straightforward sensitivity analysis is performed to show the optimal system performance for distinct outflow brine salinity conditions. We highlight that the proposed stochastic multiscenario methodology leads to better energy and economic performance solutions than a deterministic method. This is due to the fact that deterministic models cannot provide the distributions for energy consumption and process costs. For this reason, our approach represents a useful tool for supporting decision-makers towards the implementation of more robust and reliable ZLD desalination systems for treatment of shale gas flowback water.

Acknowledgements

This project has received funding from the European Union’s Horizon 2020 Research and Innovation Programme under grant agreement No. 640979.

Nomenclature

Roman letters

A	Heat transfer area, m^2
BPE	Boiling point elevation, ºC
$C^{electricity}$	Parameter for electricity cost, US\$ (kW year)$^{-1}$
C^{steam}	Parameter for steam cost, US\$ (kW year)$^{-1}$
$CAPEX$	Capital Expenditures, kUS\$ year^{-1}
Cp	Specific heat, kJ (kg ºC)$^{-1}$
C_{PO}	Cost of equipment unit, kUS\$
$CR_{\max}$	Maximum compression ratio
f_{ac}	Factor of annualized capital cost
F_{BM}	Correction factor for the capital cost
fi	Fractional interest rate per year
F_P	Parameter for the capital cost estimation
H	Specific enthalpy, kJ kg^{-1}
L_{MTD}	Logarithmic mean temperature difference
$\dot{m}$	Mass flowrate, kg s^{-1}
$\tilde{m}^{feed}$	Stochastic parameter for feeding mass flowrate, kg s^{-1}
$\bar{m}^{feed}$	Expected mean (nominal) value for feeding mass flowrate, kg s^{-1}
$OPEX$	Operational Expenses, kUS\$ year^{-1}
P	Pressure, kPa
$prob$	Probability
$\Delta P_{\min}$	Minimum pressure approach, kPa
Q	Heat flow, kW

S	Salinity, g kg^{-1}
$\tilde{S}^{feed}$	Stochastic parameter for feeding water salinity, g kg^{-1}
$\bar{S}^{feed}$	Expected mean (nominal) value for feeding water salinity, g kg^{-1}
T	Temperature, ºC
t	Retention time in the flash tanks, min
TAC	Total annualized cost, kUS$ year^{-1}
$\Delta T_{\min}$	Minimum temperature approach, ºC
U	Overall heat transfer coefficient, kW m^{-2}K^{-1}
V	Volume, m^3
X^{salt}	Salt mass fraction
W	Compression work, kW
WC	Compressor capacity, kW
y	Number of years

Subscripts

i	Evaporator effects
in	Inlet condition
out	Outlet condition
s	Scenarios

Superscript

cv	Condensate (or Distillate) vapor
is	Isentropic
mix	Mixture

S	Sensible heat
sat	Saturated vapor
sup	Superheated vapor

Acronyms

BPE	Boiling Point Elevation
CEPCI	Chemical Engineering Plant Cost Index
EC	Evaporative Crystallization
GAMS	General Algebraic Modelling System
MEE	Multiple-Effect Evaporation
MD	Membrane Distillation
MSF	Multistage Flash Distillation
MVR	Mechanical Vapor Recompression
NEA	Non-Equilibrium Allowance
NLP	Nonlinear Programming
RO	Reverse Osmosis
SEE	Single-Effect Evaporation
TVR	Thermal Vapor Recompression
ZLD	Zero-Liquid Discharge

Greek letters

γ	Heat capacity ratio
η	Isentropic efficiency
θ	Temperatures difference, ºC
κ	Thermal conductivity, kW (m K)$^{-1}$

λ	Latent heat of vaporization, kJ kg^{-1}
μ	Viscosity, kg (m s)$^{-1}$
ρ	Density, kg m^{-3}
σ	Standard deviation

References

Abraham, R., Mani, A., 2015. Heat transfer characteristics in horizontal tube bundles for falling film evaporation in multi-effect desalination system. Desalination 375, 129–137. doi:10.1016/j.desal.2015.06.018

Acharya, H.R., Henderson, C., Matis, H., Kommepalli, H., Moore, B., Wang, H., 2011. Cost effective recovery of low-TDS frac flowback water for re-use. Glob. Res. 1–100.

Al-Mutaz, I.S., Wazeer, I., 2014. Comparative performance evaluation of conventional multi-effect evaporation desalination processes. Appl. Therm. Eng. 73, 1194–1203. doi:10.1016/j.applthermaleng.2014.09.025

Boo, C., Lee, J., Elimelech, M., 2016. Omniphobic polyvinylidene fluoride (PVDF) membrane for desalination of shale gas produced water by membrane distillation. Environ. Sci. Technol. 50, 12275–12282. doi:10.1021/acs.est.6b03882

Carrero-Parreño, A., Onishi, V.C., Salcedo-Díaz, R., Ruiz-Femenia, R., Fraga, E.S., Caballero, J.A., Reyes-Labarta, J.A., 2017. Optimal pretreatment system of flowback water from shale gas production. Ind. Eng. Chem. Res. 56, 4386–4398. doi:10.1021/acs.iecr.6b04016

Chen, H., Carter, K.E., 2016. Water usage for natural gas production through hydraulic fracturing in the United States from 2008 to 2014. J. Environ. Manage. 170, 152–159. doi:10.1016/j.jenvman.2016.01.023

Chen, J.J.J., 1987. Comments on improvements on a replacement for the logarithmic mean. Chem. Eng. Sci. 42, 2488–2489. doi:10.1016/0009-2509(87)80128-8

Cho, H., Choi, Y., Lee, S., Sohn, J., Koo, J., 2016. Membrane distillation of high salinity wastewater from shale gas extraction: effect of antiscalants. Desalin. Water Treat. 57, 26718–26729. doi:10.1080/19443994.2016.1190109

Chung, H.W., Swaminathan, J., Warsinger, D.M., Lienhard V, J.H., 2016. Multistage vacuum membrane distillation (MSVMD) systems for high salinity applications. J. Memb. Sci. 497, 128–141. doi:10.1016/j.memsci.2015.09.009

Cooper, J., Stamford, L., Azapagic, A., 2016. Shale gas: A review of the economic, environmental, and social sustainability. Energy Technol. 4, 772–792. doi:10.1002/ente.201500464

Couper, J.R., Penney, W.C., Fair, J.R., Walas, S.M., 2010. Chemical process equipment, selection and design, Second Edition, USA: Elsevier.

EIA, 2016a. Annual Energy Outlook 2016 with Projections to 2040. Washington, DC: U.S. Energy Information Administration, 2016.

EIA, 2016b. International Energy Outlook 2016. Washington, DC: U.S. Energy Information Administration, 2016.

El-Dessouky, H.T., Ettouney, H.M., 1999. Multiple-effect evaporation desalination systems: Thermal analysis. Desalination 125, 259–276. doi:10.1016/S0011-9164(99)00147-2

European Commission, 2016. Eurostat.

Gao, J., You, F., 2015. Deciphering and handling uncertainty in shale gas supply chain design and optimization: Novel modeling framework and computationally efficient solution algorithm. AIChE J. 61, 3739–3755. doi:10.1002/aic.15032

Ghanbari, E., Dehghanpour, H., 2016. The fate of fracturing water: A field and simulation study. Fuel 163, 282–294. doi:10.1016/j.fuel.2015.09.040

Haluszczak, L.O., Rose, A.W., Kump, L.R., 2013. Geochemical evaluation of flowback brine from Marcellus gas wells in Pennsylvania, USA. Appl. Geochemistry 28, 55–61. doi:10.1016/j.apgeochem.2012.10.002

Hammond, G.P., O’Grady, Á., 2017. Indicative energy technology assessment of UK shale gas extraction. Appl. Energy 185, 1907–1918. doi:10.1016/j.apenergy.2016.02.024

Han, D., He, W.F., Yue, C., Pu, W.H., 2017. Study on desalination of zero-emission system based on mechanical vapor compression. Appl. Energy 185, 1490–1496. doi:10.1016/j.apenergy.2015.12.061

Hayes, T., 2009. Sampling and analysis of water streams associated with the development of Marcellus shale gas. Rep. by Gas Technol. Institute, Des Plaines, IL, Marcellus Shale Coalit. 10.

Huang, L., Fan, H., Xie, H., Huang, Z., 2016. Experimental study of treatment processes for shale gas fracturing flowback fluid in the eastern Sichuan Basin. Desalin. Water Treat. 57, 24299–24312. doi:10.1080/19443994.2016.1141714

Jacquet, J.B., 2014. Review of risks to communities from shale energy development. Environ. Sci. Technol. 48, 8321–8333. doi:10.1021/es404647x

Jang, E., Jeong, S., Chung, E., 2017. Application of three different water treatment technologies to shale gas produced water. Geosystem Eng. 20, 104–110. doi:10.1080/12269328.2016.1239553

Jiang, Q., Rentschler, J., Perrone, R., Liu, K., 2013. Application of ceramic membrane and ion-exchange for the treatment of the flowback water from Marcellus shale gas production. J. Memb. Sci. 431, 55–61. doi:10.1016/j.memsci.2012.12.030

Law, A.M., Kelton, W.D., 2000. Simulation Modeling and Analysis, 3rd ed. New York: McGraw Hill, 2000.

Lira-Barragán, L.F., Ponce-Ortega, J.M., Guillén-Gosálbez, G., El-Halwagi, M.M., 2016. Optimal water management under uncertainty for shale gas production. Ind. Eng. Chem. Res. 55, 1322–1335. doi:10.1021/acs.iecr.5b02748

Matsumoto, M., Nishimura, T., 1998. Mersenne twister: a 623-dimensionally equidistributed uniform pseudo-random number generator. ACM Trans. Model. Comput. Simul. 8, 3–30. doi:10.1145/272991.272995

Michel, M.M., Reczek, L., Granops, M., Rudnicki, P., Piech, A., 2016. Pretreatment and desalination of flowback water from the hydraulic fracturing. Desalin. Water Treat. 57, 10222–10231. doi:10.1080/19443994.2015.1038588

Onishi, V.C., Carrero-Parreño, A., Reyes-Labarta, J.A., Fraga, E.S., Caballero, J.A., 2017a. Desalination of shale gas produced water: A rigorous design approach for zero-liquid discharge evaporation systems. J. Clean. Prod. 140, 1399–1414. doi:10.1016/j.jclepro.2016.10.012

Onishi, V.C., Carrero-Parreño, A., Reyes-Labarta, J.A., Ruiz-Femenia, R., Salcedo-Díaz, R., Fraga, E.S., Caballero, J.A., 2017b. Shale gas flowback water desalination: Single vs multiple-effect evaporation with vapor recompression cycle and thermal integration. Desalination 404, 230–248. doi:10.1016/j.desal.2016.11.003

Qiu, Q., Zhu, X., Mu, L., Shen, S., 2015. Numerical study of falling film thickness over fully wetted horizontal round tube. Int. J. Heat Mass Transf. 84, 893–897. doi:10.1016/j.ijheatmasstransfer.2015.01.024

Sabio, N., Pozo, C., Guillén-Gosálbez, G., Jiménez, L., Karuppiah, R., Vasudevan, V., Sawaya, N., Farrell, J.T., 2014. Multiobjective optimization under uncertainty of the economic and life-cycle environmental performance of industrial processes. AIChE J. 60, 2098–2121. doi:10.1002/aic.14385

Sahinidis, N. V., 2004. Optimization under uncertainty: state-of-the-art and opportunities. Comput. Chem. Eng. 28, 971–983. doi:10.1016/j.compchemeng.2003.09.017

Shaffer, D.L., Arias Chavez, L.H., Ben-Sasson, M., Romero-Vargas Castrillón, S., Yip, N.Y., Elimelech, M., 2013. Desalination and reuse of high-salinity shale gas produced water: drivers, technologies, and future directions. Environ. Sci. Technol.

47, 9569–9583. doi:10.1021/es401966e

Shen, S., Mu, X., Yang, Y., Liang, G., Liu, X., 2015. Experimental investigation on heat transfer in horizontal-tube falling-film evaporator. Desalin. Water Treat. 56, 1440–1446. doi:10.1080/19443994.2014.949604

Slutz, J., Anderson, J., Broderick, R., Horner, P., 2012. Key shale gas water management strategies: an economic assessment tool. SPE/APPEA Int. Conf. Heal. Safety, Environ. Oil Gas Explor. Prod. Perth, Aust. Sept. 2012.

Smith, R.M., 2005. Chemical Process Design and Integration. Second Edition, England, John Wiley and Sons Ltd.

Stephenson, T., Valle, J.E., Riera-Palou, X., 2011. Modeling the relative GHG emissions of conventional and shale gas production. Environ. Sci. Technol. 45, 10757–10764. doi:10.1021/es2024115

Thiel, G.P., Lienhard, J.H., 2014. Treating produced water from hydraulic fracturing: Composition effects on scale formation and desalination system selection. Desalination 346, 54–69. doi:10.1016/j.desal.2014.05.001

Thu, K., Kim, Y.-D., Shahzad, M.W., Saththasivam, J., Ng, K.C., 2015. Performance investigation of an advanced multi-effect adsorption desalination (MEAD) cycle. Appl. Energy 159, 469–477. doi:10.1016/j.apenergy.2015.09.035

Tong, T., Elimelech, M., 2016. The global rise of zero liquid discharge for wastewater management: drivers, technologies, and future directions. Environ. Sci. Technol. 50, 6846–6855. doi:10.1021/acs.est.6b01000

Turton, Bailie, R.C., Whiting, W.B., 2012. Analysis , Synthesis , and Design of Chemical Processes, fourth ed.

Vengosh, A., Jackson, R.B., Warner, N., Darrah, T.H., Kondash, A., 2014. A critical review of the risks to water resources from unconventional shale gas development and hydraulic fracturing in the United States. Environ. Sci. Technol. 48, 8334–8348. doi:10.1021/es405118y

Vengosh, A., Warner, N., Jackson, R., Darrah, T., 2013. The effects of shale gas exploration and hydraulic fracturing on the quality of water resources in the United States. Procedia Earth Planet. Sci. 7, 863–866. doi:10.1016/j.proeps.2013.03.213

Vidic, R.D., Brantley, S.L., Vandenbossche, J.M., Yoxtheimer, D., Abad, J.D., 2013. Impact of shale gas development on regional water quality. Science (80) 340, 1235009–1235009. doi:10.1126/science.1235009

Wächter, A., Biegler, L.T., 2006. On the implementation of an interior-point filter line-search algorithm for large-scale nonlinear programming. Math. Program. 106, 25–57. doi:10.1007/s10107-004-0559-y

Xiong, B., Zydney, A.L., Kumar, M., 2016. Fouling of microfiltration membranes by flowback and produced waters from the Marcellus shale gas play. Water Res. 99, 162–170. doi:10.1016/j.watres.2016.04.049

Yang, L., Grossmann, I.E., Manno, J., 2014. Optimization models for shale gas water management. AIChE J. 60, 3490−3501. doi:10.1002/aic.14526

Zammerilli, A., Murray, R.C., Davis, T., Littlefield, J., 2014. Environmental impacts of unconventional natural gas development and production DOE/NETL-2014/1651, 800, 553−7681.

Zhang, X., Sun, A.Y., Duncan, I.J., 2016. Shale gas wastewater management under uncertainty. J. Environ. Manage. 165, 188–198. doi:10.1016/j.jenvman.2015.09.038

List of Figure Captions

Fig. 1. General superstructure proposed for the MEE-MVR desalination plant of flowback water from shale gas production. This figure is adapted from Onishi et al. (2017b).

Fig. 2. Decision variables for the optimization of: (*a*) single-stage compressor; and, (*b*) effect *i* of the horizontal falling film evaporator coupled to flashing tank *i* in the MEE-MVR system.

Fig. 3. Optimal configuration and operational conditions obtained for the multiple-effect evaporation system with mechanical vapor recompression (MEE-MVR) through the deterministic approach.

Fig. 4. Energy consumption distribution throughout the different feeding scenarios, obtained via stochastic approach with fixed equipment capacities as provided by the deterministic solution.

Fig. 5. Freshwater cost distribution throughout the different feeding scenarios, obtained via stochastic approach with fixed equipment capacities as provided by the deterministic solution.

Fig. 6. Correlated feeding scenarios generated with marginal normal distribution, considering matrix correlation of - 0.8 and standard deviation of 10% from expected mean values.

Fig. 7. Optimal MEE-MVR system configuration obtained by the proposed stochastic modelling approach.

Fig. 8. Distributions of freshwater production cost and produced freshwater obtained by the stochastic model throughout the distinct feeding scenarios.

Fig. 9. Cumulative probability curves for the system economic performance under consideration of weakly correlated uncertain parameters (matrix correlation factor of 0.1).

Fig. 10. Cumulative probability curves for the system economic performance under consideration of strongly correlated uncertain parameters (matrix correlation of 0.9).

Appendix A. Correlations for estimating fluid physical properties and boiling point elevation (BPE)

A.1 Fluid physical properties

The thermodynamic properties of the fluids are estimated for each feeding scenario *s* via correlations obtained from process simulations in Aspen HYSYS-OLI, considering the thermodynamic package for electrolytes. The correlations are valid for salt concentrations ranging between $0 \le X_{i,s}^{salt} \le 0.3$, and temperature in a range of $10 \le T_{i,s}\left({}^{\circ}\mathrm{C}\right) \le 120$.

The correlations for the estimation of the fluid physical properties in the scenario *s* are presented as follows.

Thermal conductivity. Fluids thermal conductivity $\kappa_{i,s}$ in the effect *i* of the evaporator is estimated by the **Eq. (A.1)**.

$$\kappa_{i,s} = 0.001 \cdot \left[0.561 + 0.0017 \cdot \left(T_{i,s}\right) - 0.00000612 \cdot \left(T_{i,s}\right)^2 \right] \quad \forall i \in I,\ \forall s \in S \qquad \text{(A.1)}$$

In which the fluid temperature $T_{i,s}$ is given in ºC and the conductivity $\kappa_{i,s}$ is in kW (m K)$^{-1}$.

Viscosity. Fluids viscosity $\mu_{i,s}$ in each evaporation effect *i* is given by the following correlation.

$$\mu_{i,s} = 0.001 \cdot \begin{bmatrix} 1.377 + 1.845 \cdot \left(X_{i,s}^{salt} \right) - 0.02301 \cdot \left(T_{i,s} \right) + 7.475 \cdot \left(X_{i,s}^{salt} \right)^2 \\ -\ 0.03427 \cdot \left(X_{i,s}^{salt} \cdot T_{i,s} \right) + 0.0001418 \cdot \left(T_{i,s} \right)^2 \end{bmatrix} \quad \forall i \in I,\ \forall s \in S \tag{A.2}$$

In which, $X_{i,s}^{salt}$ indicates the salt mass fraction ($X_{i,s}^{salt} = 0.001 \cdot S_{i,s}^{brine}$), while $T_{i,s}$ indicates the streams temperature in the effect *i* of evaporation. The temperature $T_{i,s}$ is expressed in ºC and the viscosity $\mu_{i,s}$ is obtained in kg (m s)$^{-1}$.

Specific heat. Fluids specific heat $Cp_{i,s}$ is calculated by accounting for the influence of the streams salt concentration and temperature in each evaporator effect *i*, as shown in **Eq. (A.3)**.

$$Cp_{i,s} = 4.118 - 4.757 \cdot \left(X_{i,s}^{salt} \right) + 0.001015 \cdot \left(T_{i,s} \right) \quad \forall i \in I,\ \forall s \in S \tag{A.3}$$

In which the fluid temperature $T_{i,s}$ is given in ºC and their specific heat $Cp_{i,s}$ is expressed in kJ (kg ºC)$^{-1}$.

Density. Streams density $\rho_{i,s}$ in an evaporation effect *i* is estimated by the next correlation.

$$\rho_{i,s} = 1016 + 719.6 \cdot \left(X_{i,s}^{salt} \right) - 0.672 \cdot \left(T_{i,s} \right) \quad \forall i \in I,\ \forall s \in S \tag{A.4}$$

In which, $\rho_{i,s}$ is given in kg m^{-3}, while $T_{i,s}$ is expressed in ºC.

The fluids physical properties expressed by **Eq. (A.1)** to **Eq. (A.4)** are calculated for the streams liquid phase at the temperatures of evaporation ($T_{i,s}^{boiling}$) and condensation ($T_{i,s}^{condensate}$). For the estimation of the thermodynamic properties of the condensate inside the horizontal-tubes, we consider salt free streams ($X_{i,s}^{salt} = 0$).

Vaporization latent heat. Latent heat of vaporization $\lambda_{i,s}$ of the streams in each evaporation effect *i* is obtained by the following equation.

$$\lambda_{i,s} = 2502.5 - 2.3648 \cdot \left(T_{i,s}^{sat}\right) + 1.840 \cdot \left(T_{i-1,s}^{sat} - T_{i,s}^{sat}\right) \qquad \forall i > 1,\ \forall s \in S \tag{A.5}$$

In which, $\lambda_{i,s}$ is given in kJ kg^{-1}. $T_{i,s}^{sat}$ is the saturated vapor temperature expressed in °C. This temperature is calculated by the Antoine Equation for vapor-liquid equilibrium:

$$\ln\left(P_{i,s}^{sat}\right) = A + B\Big/\left(T_{i,s}^{sat} + C\right) \qquad \forall i \in I,\ \forall s \in S \tag{A.6}$$

In which, $P_{i,s}^{sat}$ is the streams pressure of saturation given in kPa. In addition, *A*, *B* and *C* are the Antoine parameters that assume the values of 12.98437, -2001.77468, and 139.61335, respectively.

Note that **Eq. (A.6)** also permits the determination of the ideal temperature $T_{i,s}^{ideal}$ (corresponding to the temperature that the evaporation effect *i* would have for the salt concentration equal to zero) in the effect *i* of the evaporator. In this case, the vapor pressure $P_{i,s}^{vapor}$ should be considered in **Eq. (A.6)**.

Specific enthalpies. Vapor and liquid specific enthalpies ($H_{i,s}^{vapor}$ and $H_{i,s}^{liquid}$, respectively) of the streams in each evaporation effect *i* are estimated as follows.

$$H_{i,s}^{vapor} = -13470 + 1.840 \cdot \left(T_{i,s}^{boiling} \right) \quad \forall i \in I, \ \forall s \in S \tag{A.7}$$

$$H_{i,s}^{liquid} = -15940 + 8787 \cdot \left(X_{i,s}^{salt} \right) + 3.557 \cdot \left(T_{i,s}^{boiling} \right) \quad \forall i \in I, \ \forall s \in S \tag{A.8}$$

In which, $H_{i,s}$ is obtained in kJ kg^{-1}, whereas the boiling temperature $T_{i,s}^{boiling}$ is given in ºC. The specific enthalpy for the feed water (*i.e.*, shale gas flowback water) in the last evaporation effect *I* can be obtained by **Eq. (A.8)**, considering its inlet salt mass fraction (X_{in}^{feed}) and temperature (T_{in}^{feed}). Still, we consider the temperature $T_{i,s}^{condensate}$ and $X_{i,s}^{salt} = 0$ in **Eq. (A.8)** for estimating condensate specific enthalpies inside tubes.

A.2 Boiling point elevation (BPE)

The boiling point elevation ($BPE_{i,s}$) is related to the raise in the boiling point temperature due to the brine salt concentration. The BPE can be estimated as a function of the ideal temperature and salt mass fraction inside the *i*-effect of evaporation for each feeding scenario *s*, as shown in **Eq. (A.9)**.

$$BPE_{i,s} = \begin{bmatrix} 0.1581 + 2.769 \cdot \left(X_{i,s}^{salt} \right) - 0.002676 \cdot \left(T_{i,s}^{ideal} \right) \\ + \ 41.78 \left(X_{i,s}^{salt} \right)^{0.5} + 0.134 \cdot \left(X_{i,s}^{salt} \cdot T_{i,s}^{ideal} \right) \end{bmatrix} \quad \forall i \in I, \ \forall s \in S \tag{A.9}$$

In which,

$$X_{i,s}^{salt} = 0.001 \cdot \left(S_{i,s}^{brine} \right) \quad \forall i \in I, \ \forall s \in S \tag{A.10}$$

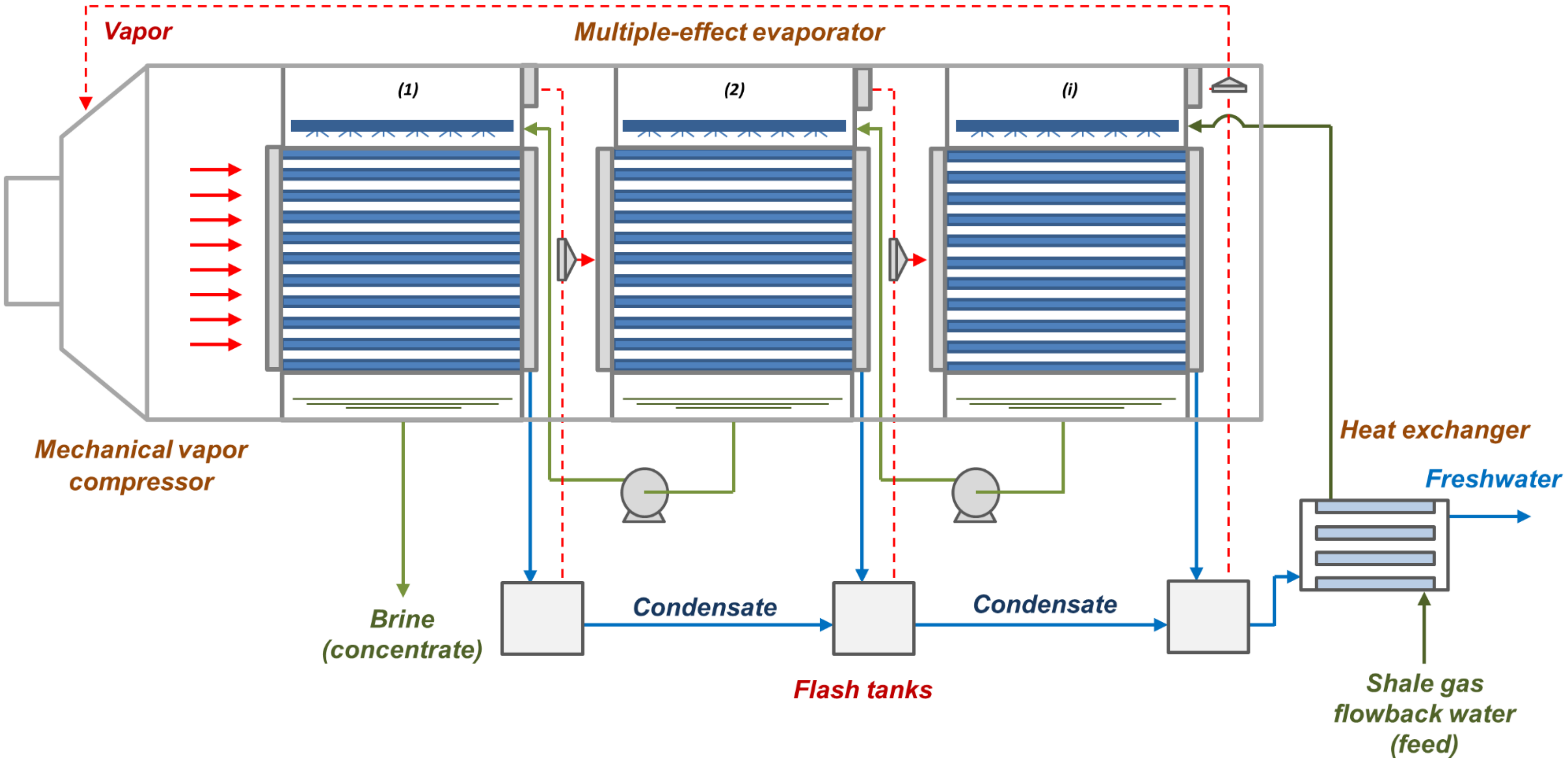

Fig. 1. General superstructure proposed for the MEE-MVR desalination plant of flowback water from shale gas production. This figure is adapted from Onishi et al. (2017b).

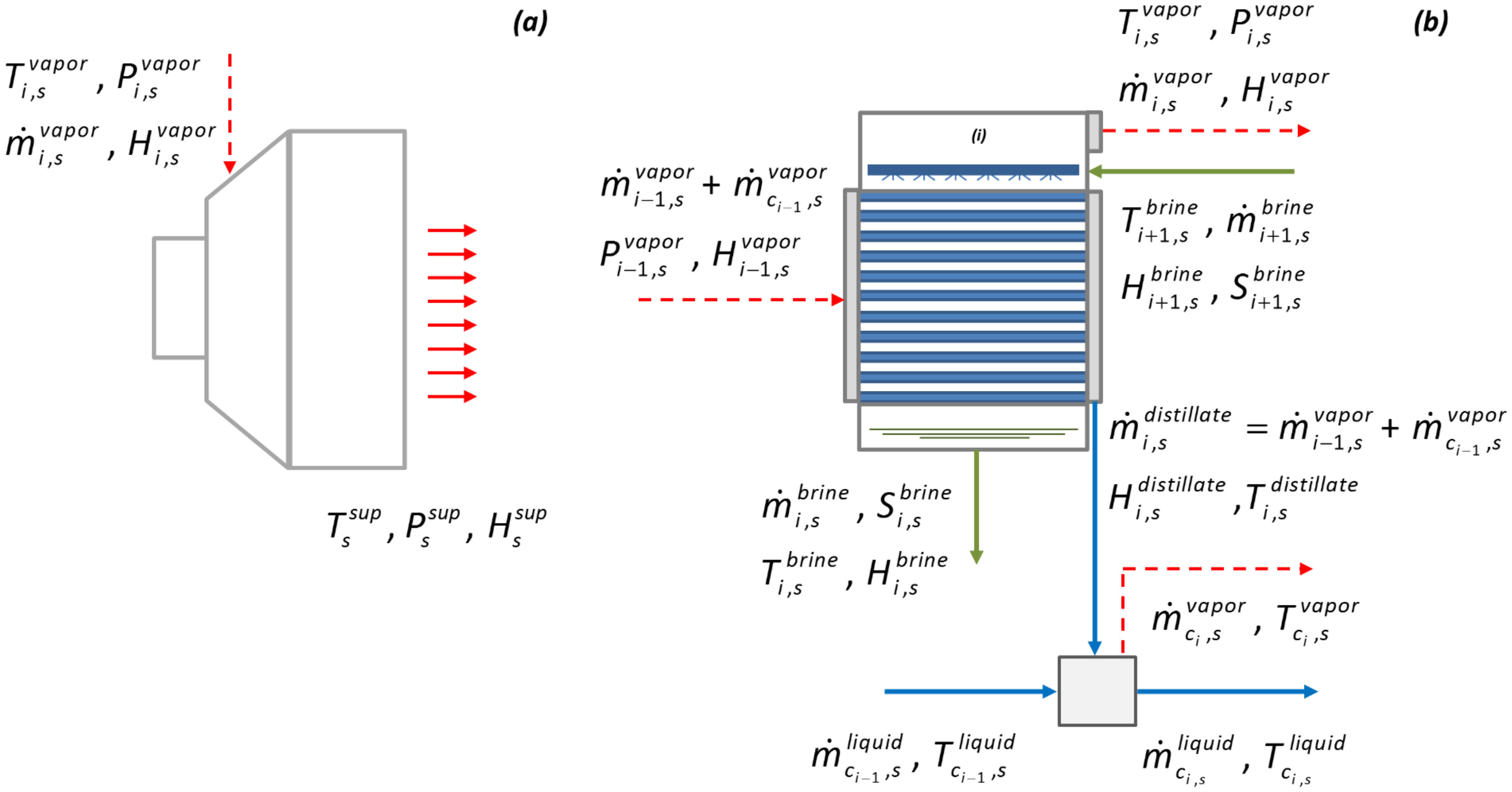

Fig. 2. Decision variables for the optimization of: (*a*) single-stage compressor; and, (*b*) effect *i* of the horizontal falling film evaporator coupled to flashing tank *i* in the MEE-MVR system.

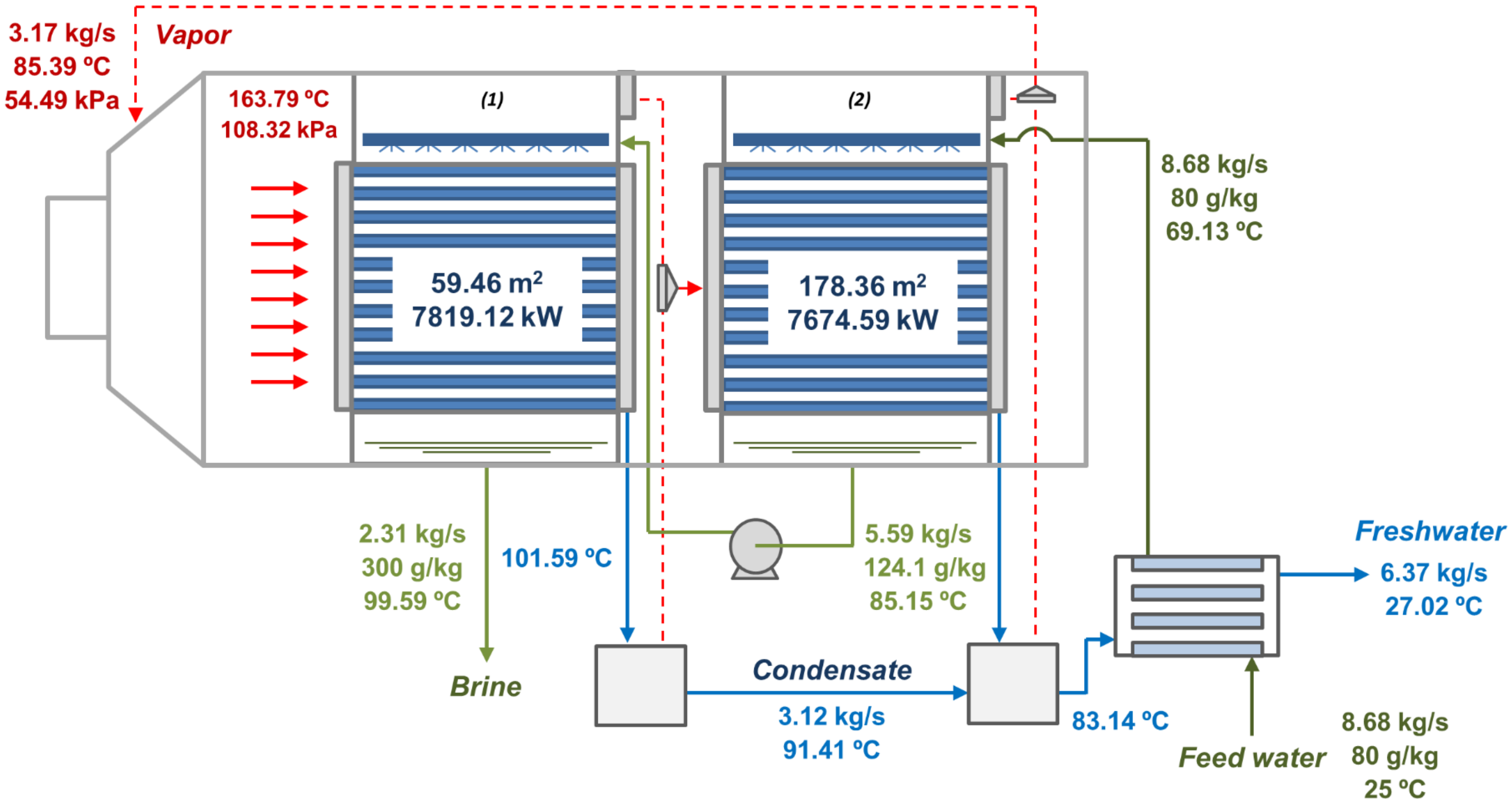

Fig. 3. Optimal configuration and operational conditions obtained for the multiple-effect evaporation system with mechanical vapor recompression (MEE-MVR) through the deterministic approach.

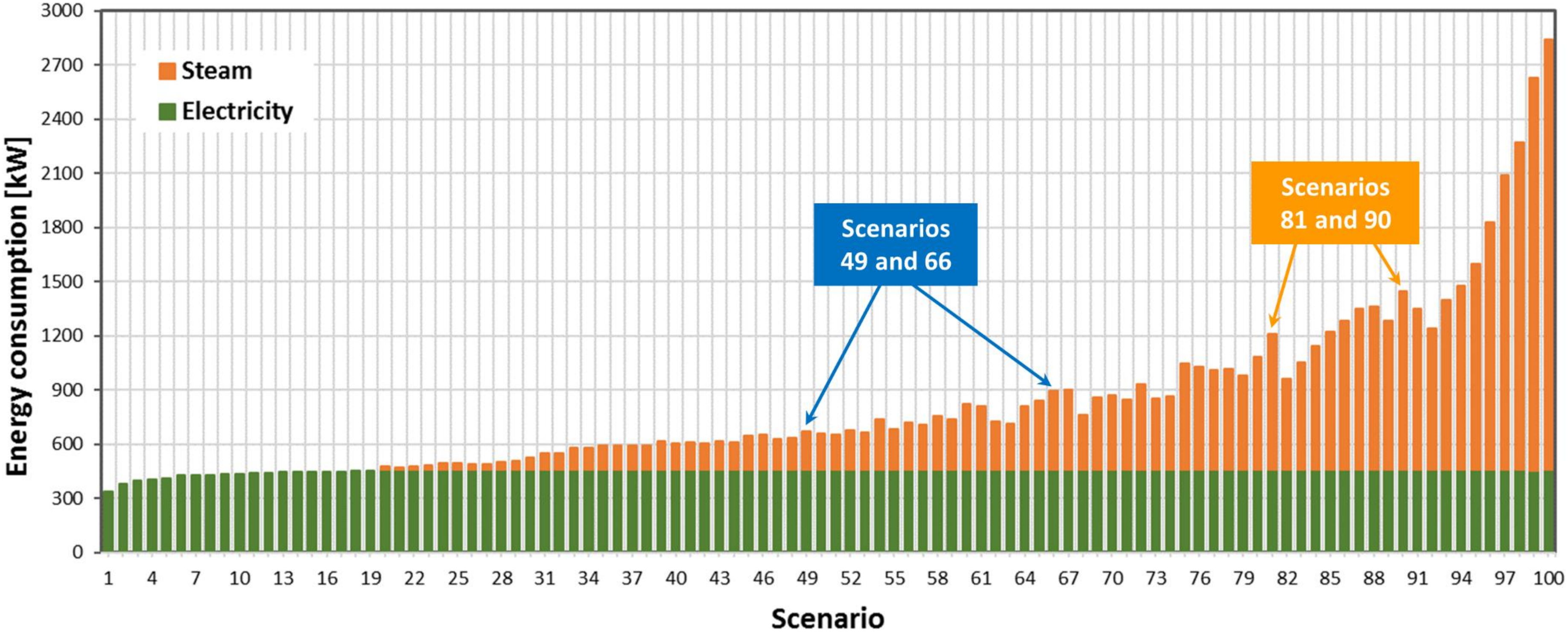

Fig. 4. Energy consumption distribution throughout the different feeding scenarios, obtained via stochastic approach with fixed equipment capacities as provided by the deterministic solution.

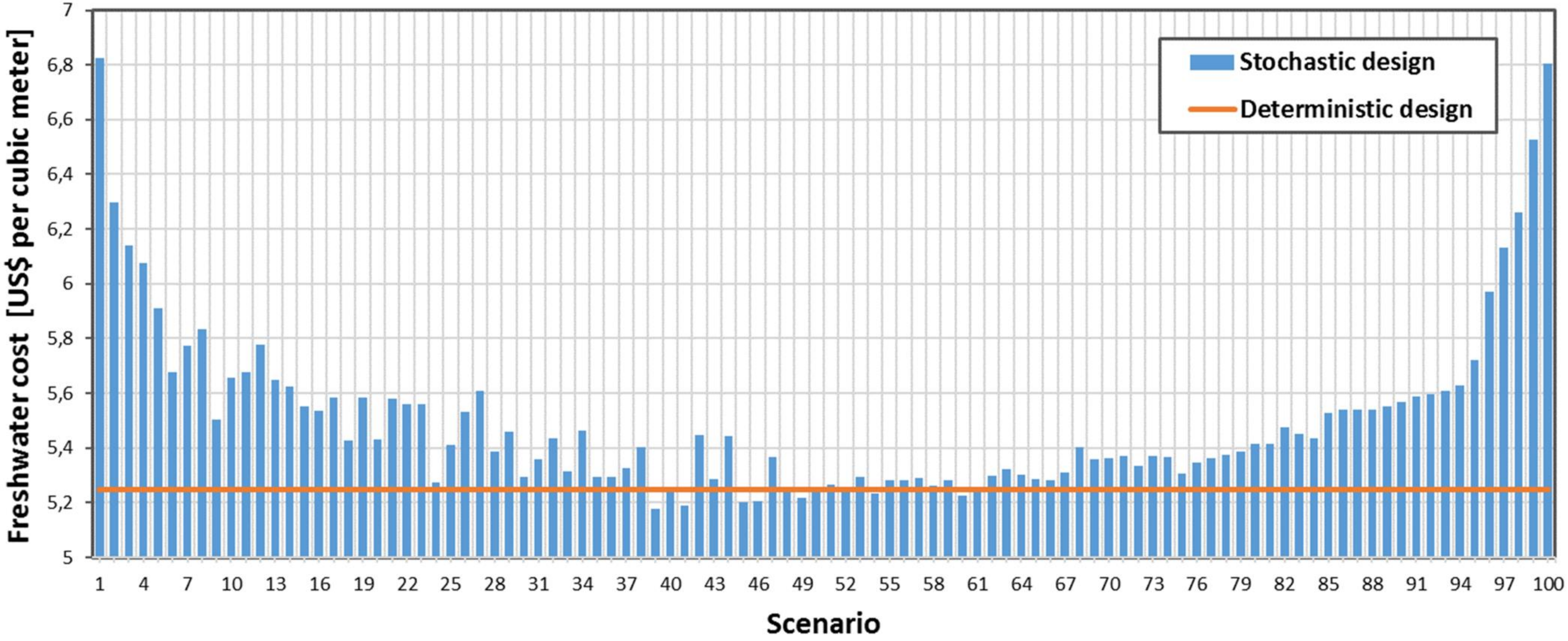

Fig. 5. Freshwater cost distribution throughout the different feeding scenarios, obtained via stochastic approach with fixed equipment capacities as provided by the deterministic solution.

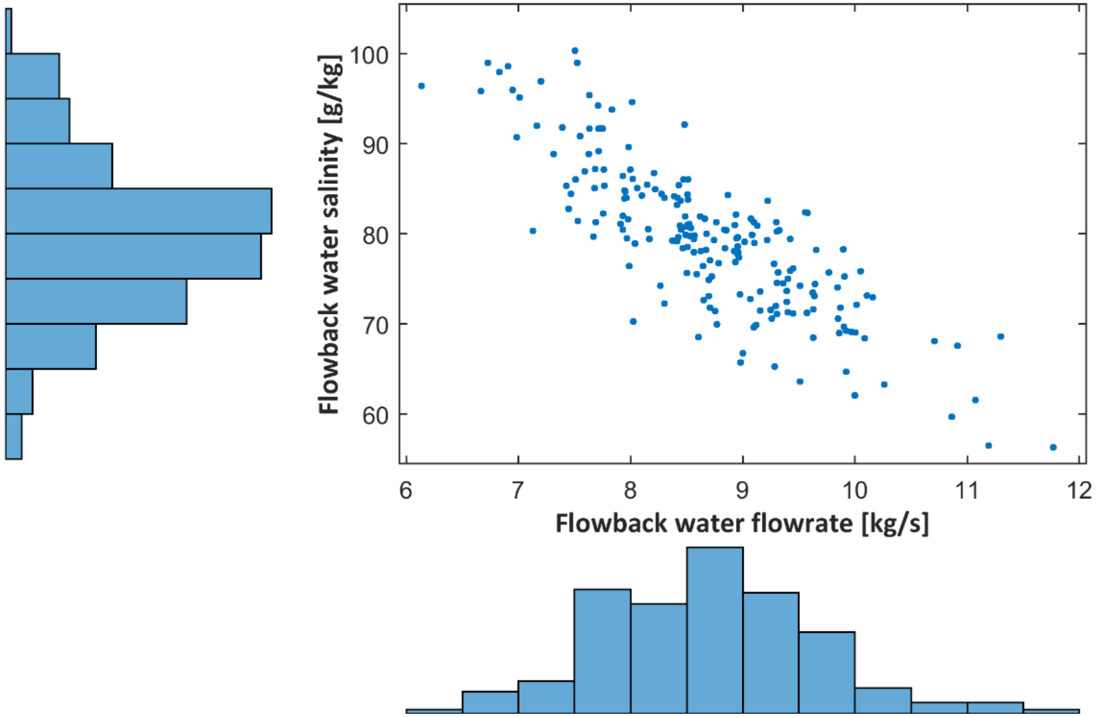

Fig. 6. Correlated feeding scenarios generated with marginal normal distribution, considering matrix correlation of - 0.8 and standard deviation of 10% from expected mean values.

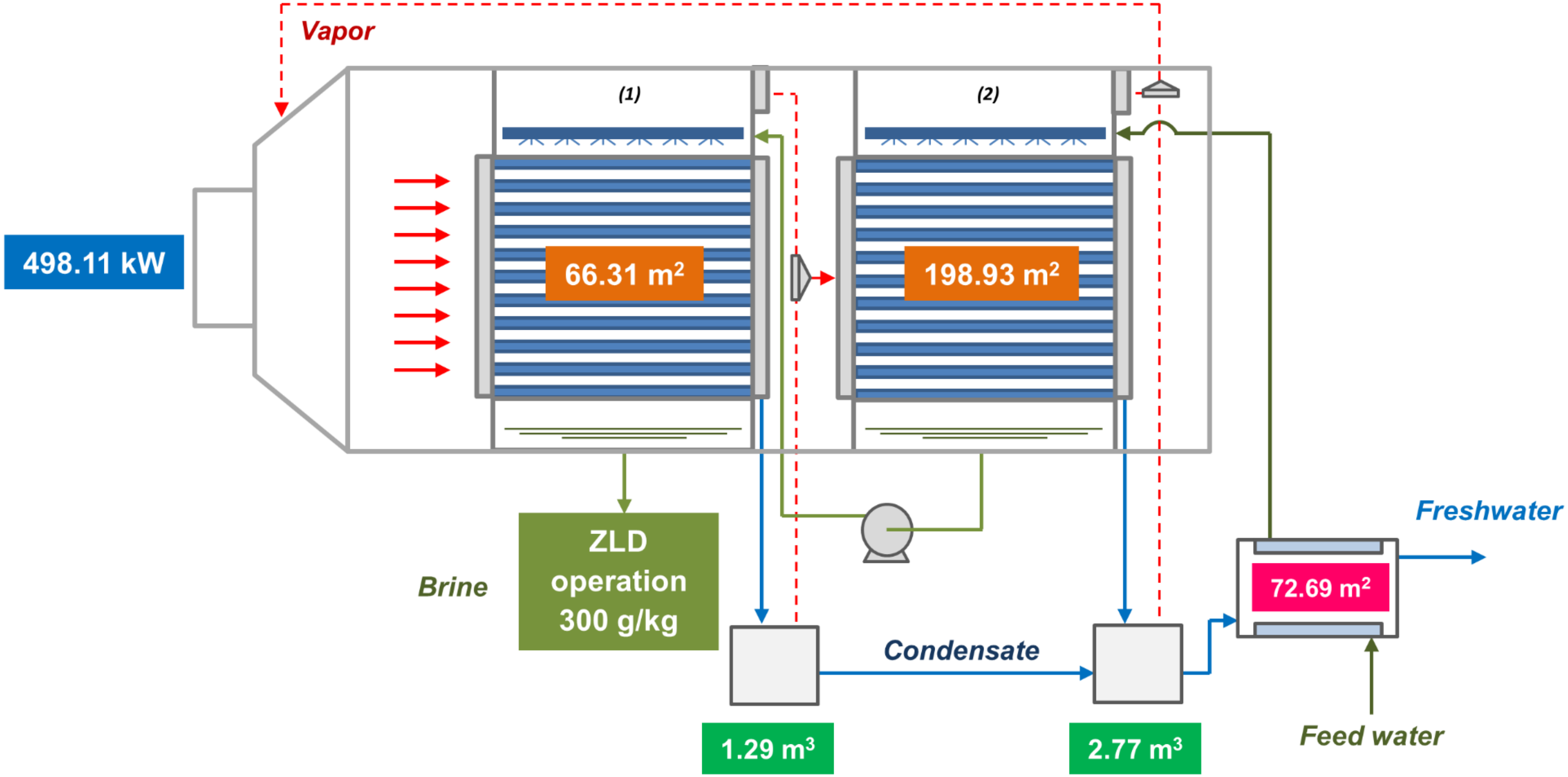

Fig. 7. Optimal MEE-MVR system configuration obtained by the proposed stochastic modelling approach.

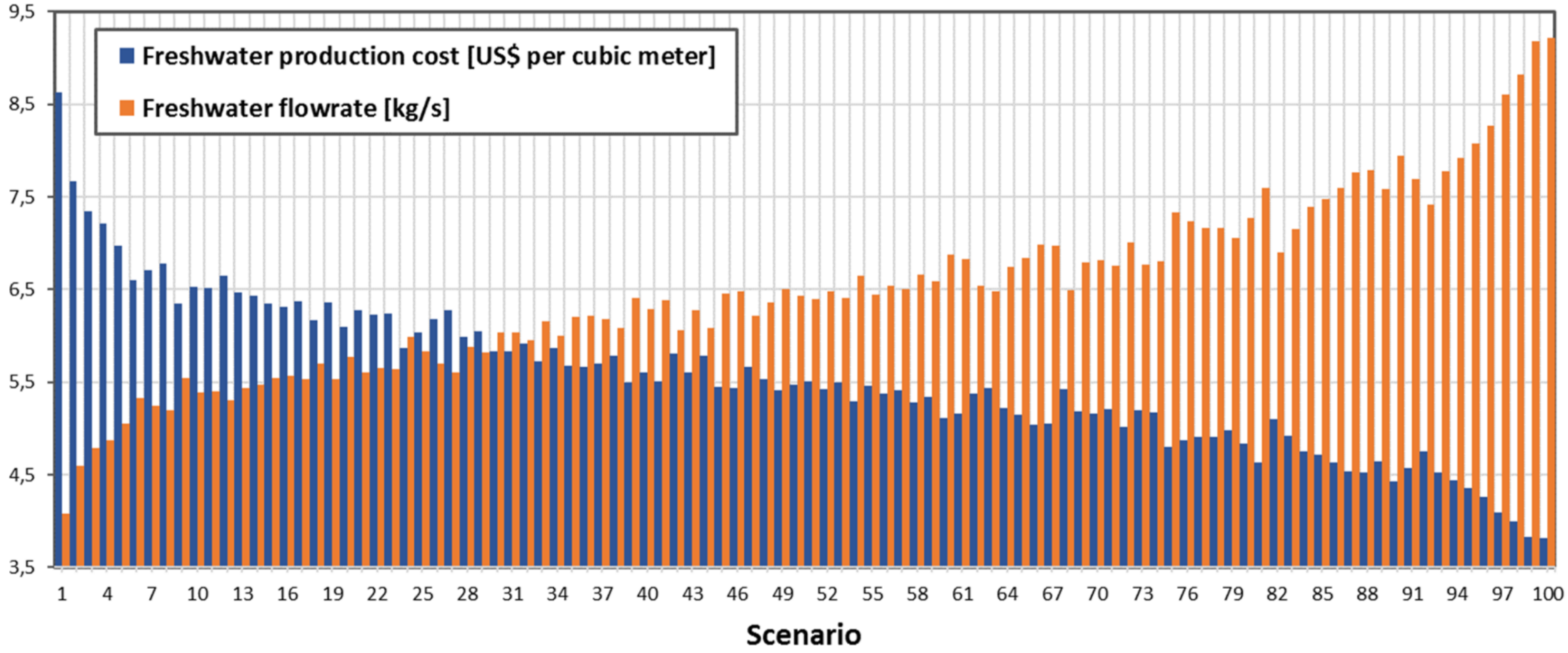

Fig. 8. Distributions of freshwater production cost and produced freshwater obtained by the stochastic model throughout the distinct feeding scenarios.

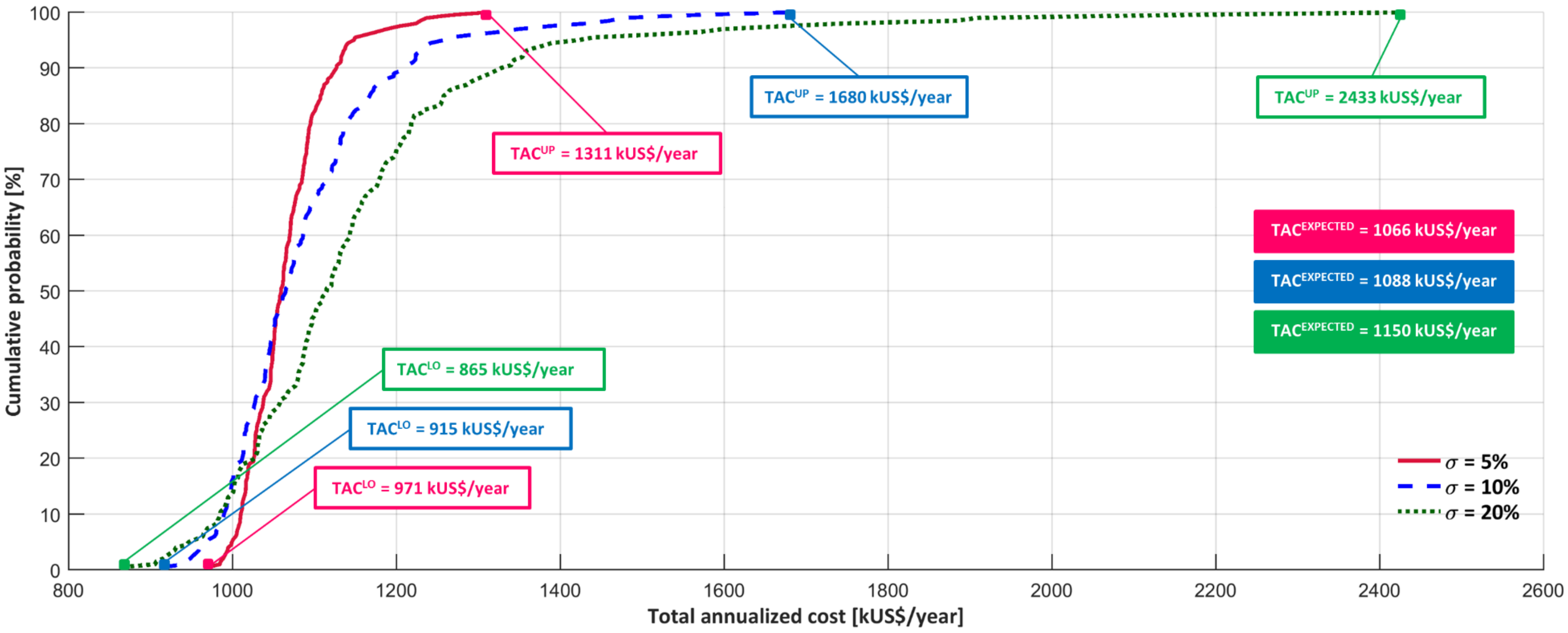

Fig. 9. Cumulative probability curves for the system economic performance under consideration of weakly correlated uncertain parameters (matrix correlation factor of 0.1).

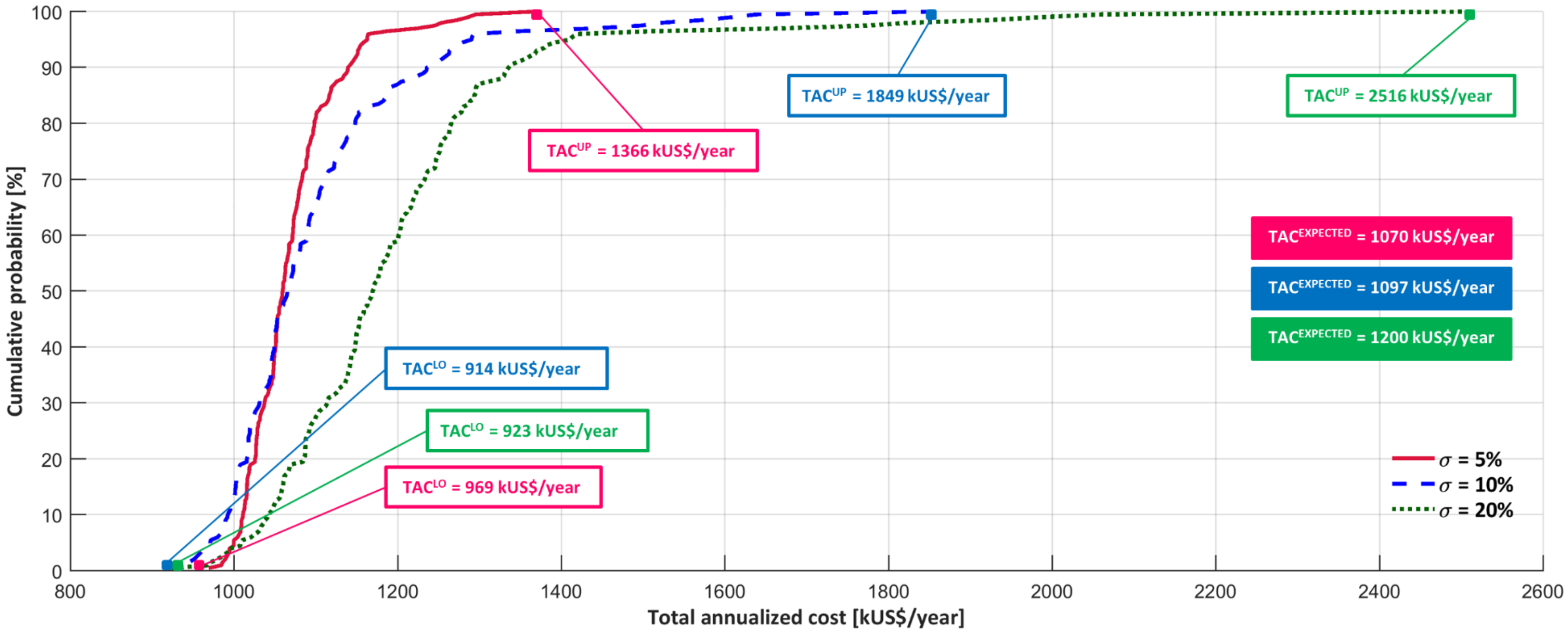

Fig. 10. Cumulative probability curves for the system economic performance under consideration of strongly correlated uncertain parameters (matrix correlation of 0.9).

Table 1

Shale gas flowback water data and water amount required for drilling and fracturing processes in important U.S. shale plays.

Report	**U.S. Shale play**	**Average TDS (k ppm)**	**Water amount (m^3)**	**Flowback water (%)**
Acharya et al. (2011)	Fayetteville	13	11368 [a]	15−40% [b]
	Woodford	30	-	
	Barnett	80	12719 [a]	
	Marcellus	120	14627 [a]	
	Haynesville	110	14309 [a]	
Hayes (2009)	Marcellus	-	11356−15142	25%
Haluszczak et al. (2013)	Marcellus	157 [c]	-	25%
Thiel and Lienhard V (2014)	Marcellus	145	-	-
Zammerilli et al. (2014)	Marcellus	70	7570−22712	30−70%
Slutz et al. (2012)	-	-	12700−19000	10−40%
Vidic et al. (2013)	Marcellus	-	7570−26500	9−53%
Hammond and O’Grady (2017)	-	-	10000−30000	40−80%

[a] *Average values.*

[b] *Overall produced water recovery after 90 days.*

[c] *TDS average values for the shale gas flowback water in 14th day of hydraulic fracturing.*

Table 2

Problem data for the case study regarding the optimal design of MEE-MVR desalination systems under well data uncertainty.

Feed water	Expected mean value for mass flowrate, $\bar{m}_I^{feed}$ (kg s^{-1})	8.68
	Temperature, T_I^{feed} (ºC)	25
	Expected mean value for salinity, $\bar{S}_I^{feed}$ (g kg^{-1} or k ppm)	80
Mechanical vapor compressor	Isentropic efficiency, η_s (%)	50–85
	Heat capacity ratio, γ	1.33
	Maximum compression ratio, $CR_{\max}$	3
Process specification and restrictions	Brine salinity for ZLD operation, S^{design} (g kg^{-1} or k ppm)	300
	Maximum effect temperature, T_i^{ideal} (ºC)	100

	Maximum effect pressure, P_i^{sat} (kPa)	200
Cost data	Electricity cost ^{a}, $C^{electricity}$ (US$ (kW year)$^{-1}$)	850.51
	Steam cost, C^{steam} (US$ (kW year)$^{-1}$)	418.80
	Fractional interest rate per year, i	0.1
	Amortization period, y	10
	Working hours for year	8760

[a] *Cost data obtained from Eurostat database* (European Commission, 2016) *(1st semester – 2015).*

Supporting Information

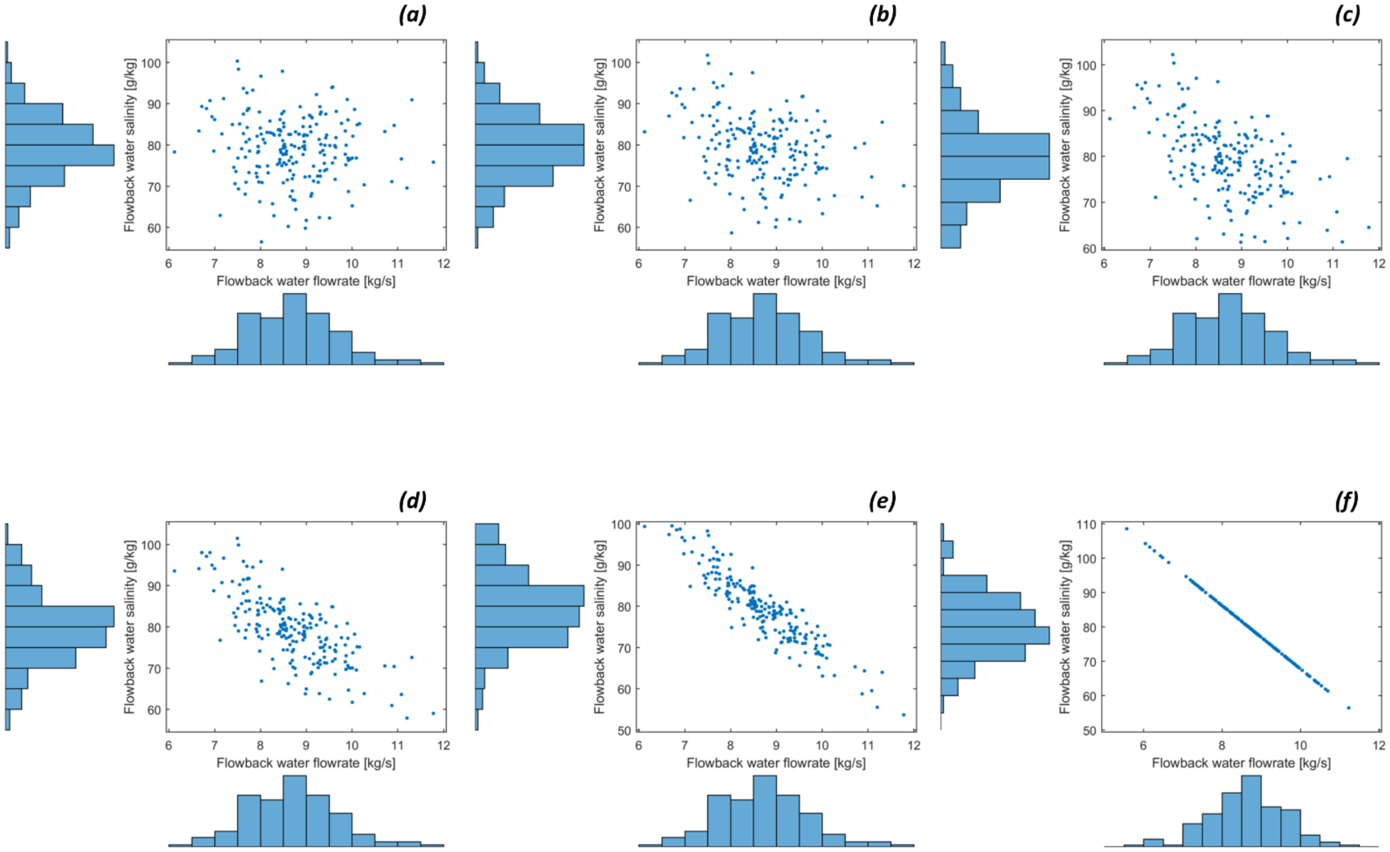

Fig. S1. Correlated feeding scenarios generated with marginal normal distributions, considering the diagonal-off element of the correlation matrix equal to: (*a*) - 0.1; (*b*) - 0.3; (*c*) - 0.5; (*d*) - 0.7; (*e*) - 0.9; and, (*f*) - 1 (well data are completely correlated). In all cases, 200 scenarios are generated with standard deviation of 10% from expected mean values.

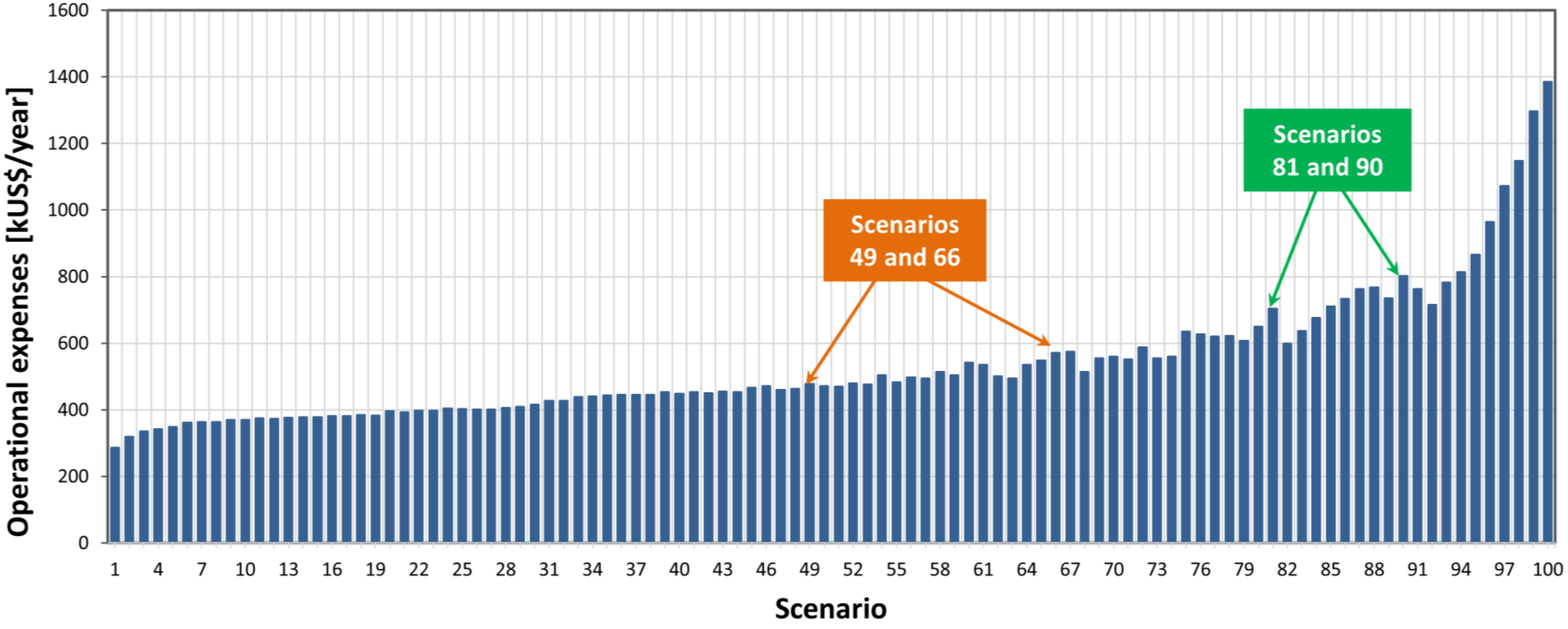

Fig. S2. Operational expenses distribution throughout the different feeding scenarios, obtained via stochastic approach with fixed equipment capacities as provided by the deterministic solution.

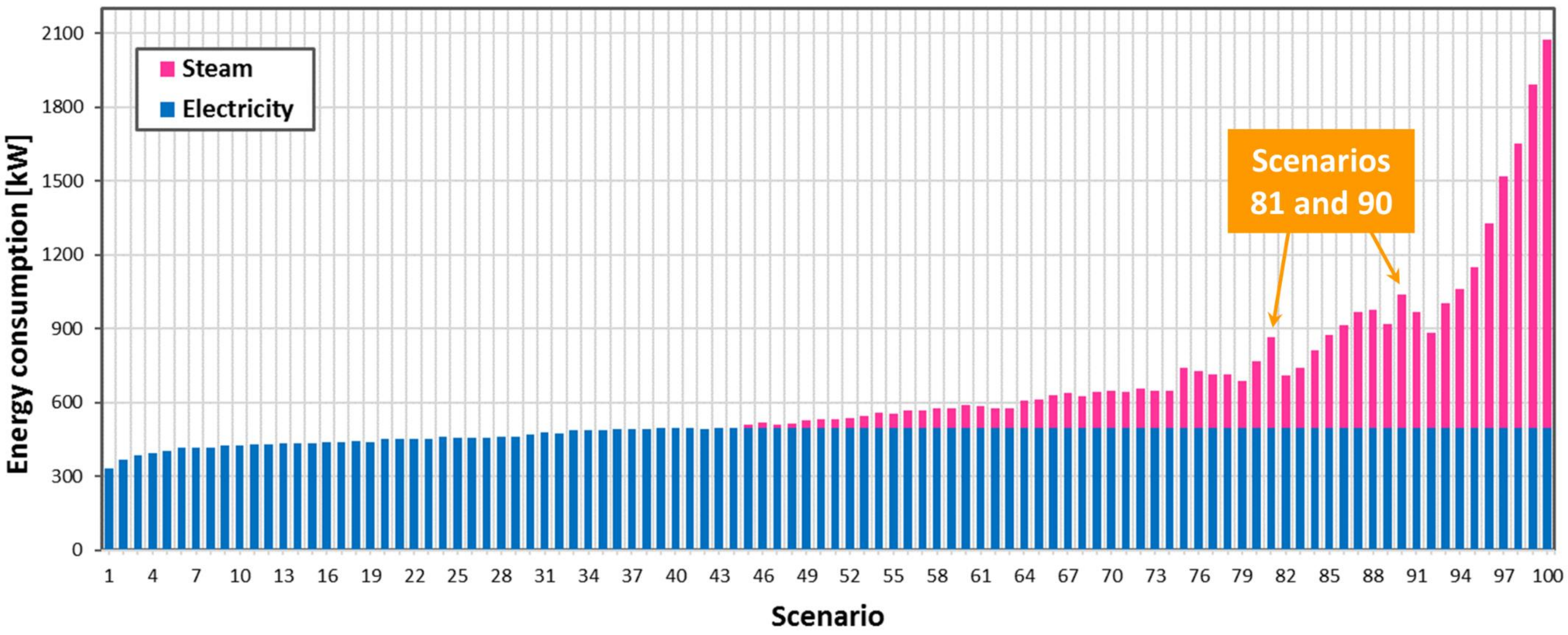

Fig. S3. Distribution for energy consumption obtained by the stochastic model throughout the different feeding scenarios.

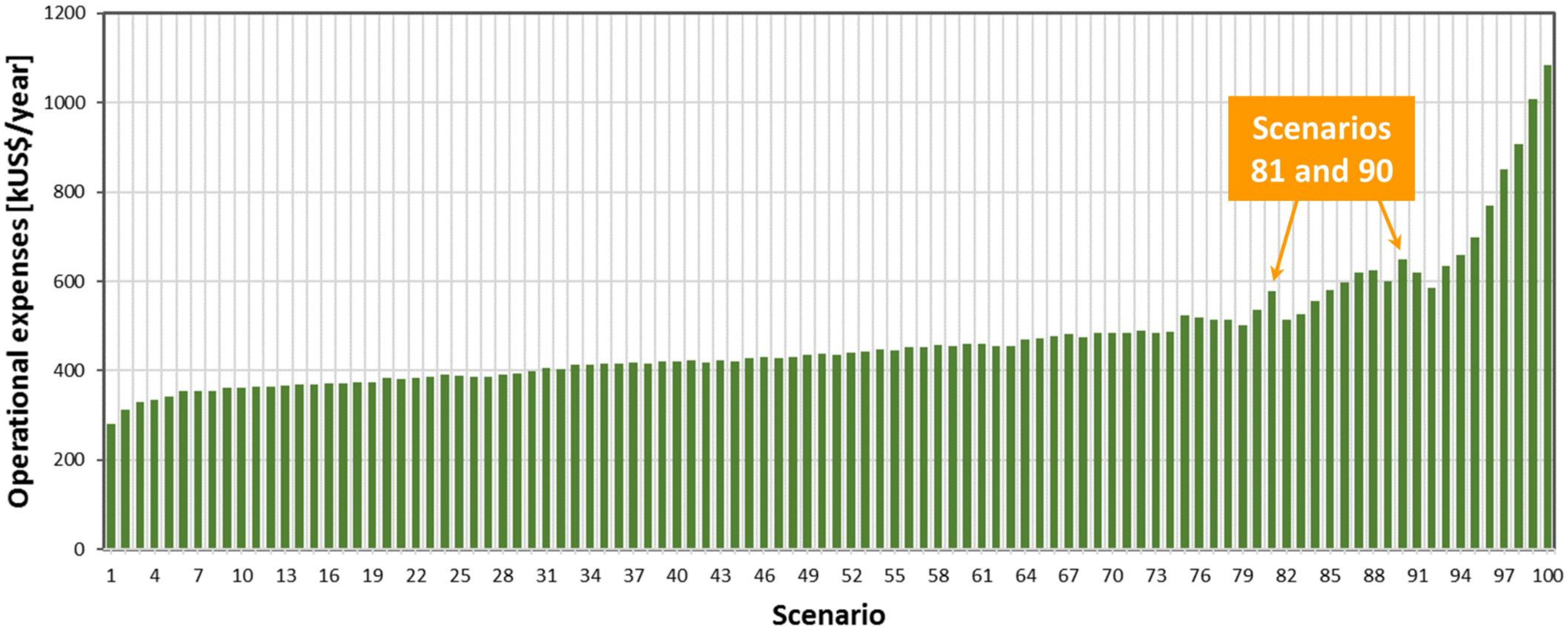

Fig. S4. Distribution for operational expenses obtained by the stochastic model throughout the different feeding scenarios.

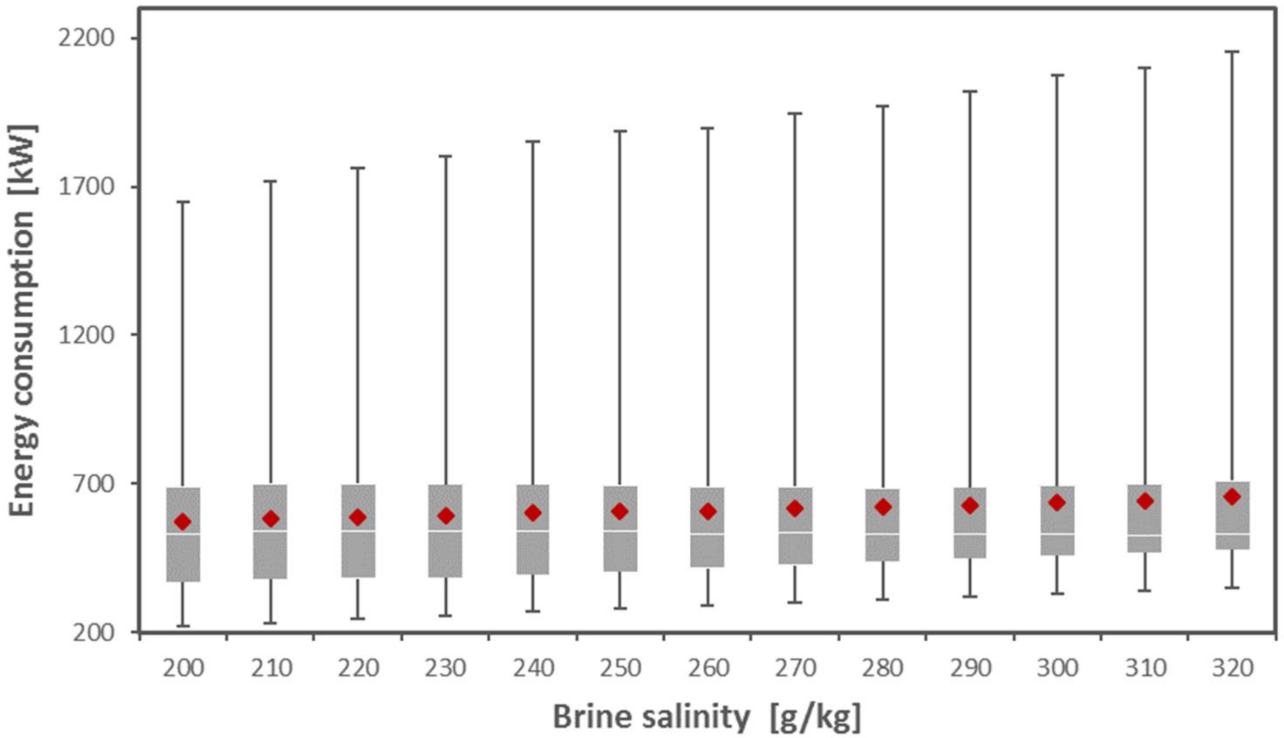

Fig. S5. Box and whisker plot for energy consumption according to brine salinity at discharge. ♦ indicates the expected value (100 scenarios).

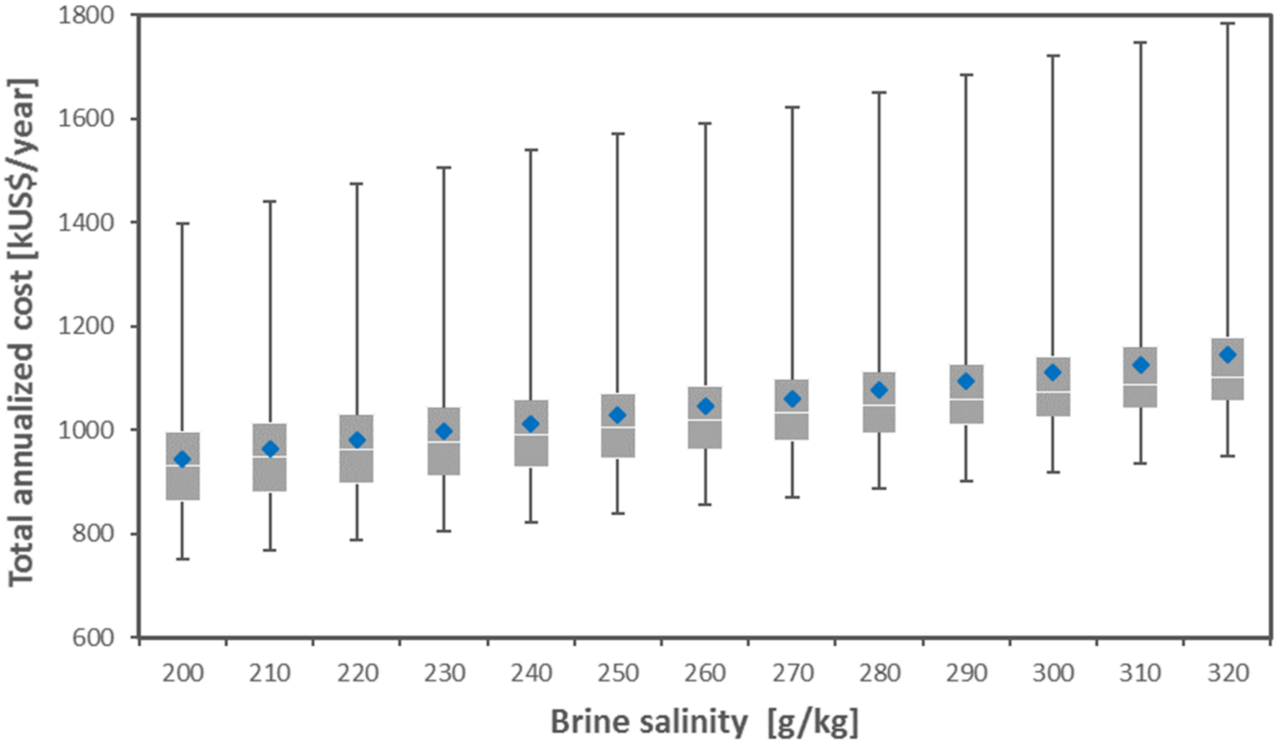

Fig. S6. Box and whisker plot for total annualized cost according to brine salinity at discharge. ♦ indicates the expected value (100 scenarios).